Mu2e experiment
Search for Charged Lepton Flavour Violation

Namitha Chithirasreemadam
namitha@pi.infn.it

UNIVERSITÀ DI PISA
INFN, PISA

Probes Annual General Meeting

November 23, 2025

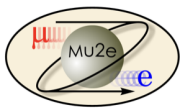



Charged Lepton Flavour Violation (CLFV)

- Flavor is not conserved in:

Charged Lepton Flavour Violation (CLFV)

- Flavor is not conserved in:
  1. Quarks (quark mixing, CKM matrix)

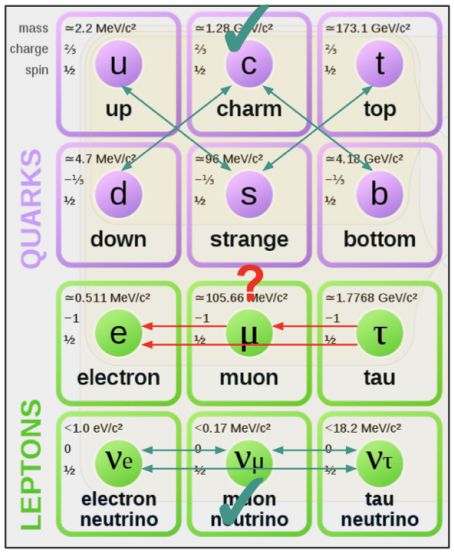

Charged Lepton Flavour Violation (CLFV)

- Flavor is not conserved in:
  1. Quarks (quark mixing, CKM matrix)
  2. Neutrinos (neutrino oscillations, PMNS matrix)

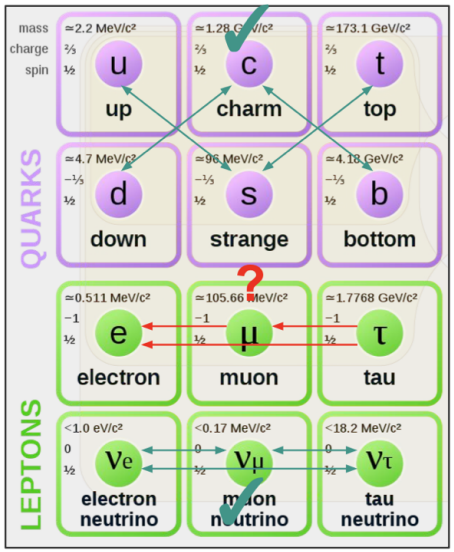

Charged Lepton Flavour Violation (CLFV)

- Flavor is not conserved in:
  1. Quarks (quark mixing, CKM matrix)
  2. Neutrinos (neutrino oscillations, PMNS matrix)
  3. Charged leptons ?

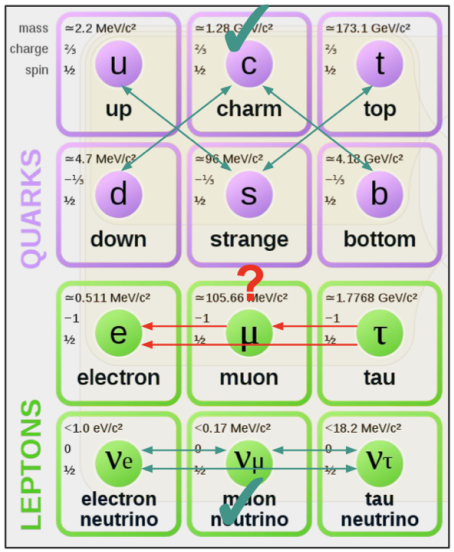

Charged Lepton Flavour Violation (CLFV)

- Flavor is not conserved in:
  1. Quarks (quark mixing, CKM matrix)
  2. Neutrinos (neutrino oscillations, PMNS matrix)
  3. Charged leptons ?
- CLFV processes can occur through neutrino oscillation.

$$BR(\mu \to e\gamma) = \frac{3\alpha}{32\pi}(\frac{1}{4})sin^2 2\theta_{13} sin^2\theta_{23} |\frac{\Delta m^2_{13}}{M^2_W}|^2$$

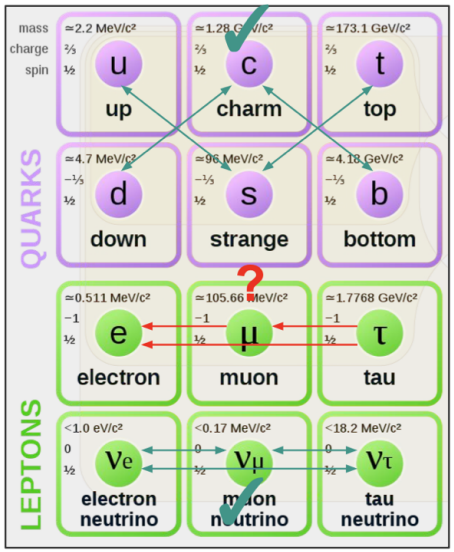

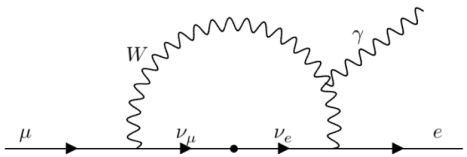

Charged Lepton Flavour Violation (CLFV)

- Flavor is not conserved in:
  1. Quarks (quark mixing, CKM matrix)
  2. Neutrinos (neutrino oscillations, PMNS matrix)
  3. Charged leptons ?
- CLFV processes can occur through neutrino oscillation.

$$BR(\mu \to e\gamma) = \frac{3\alpha}{32\pi}(\frac{1}{4})sin^2 2\theta_{13} sin^2\theta_{23} |\frac{\Delta m^2_{13}}{M^2_W}|^2$$

- BR of CLFV processes through neutrino oscillations are suppressed by factors proportional to $(\Delta m^2_\nu)^2/M^4_W$ to undetectably tiny levels, $< 10^{-50}$.

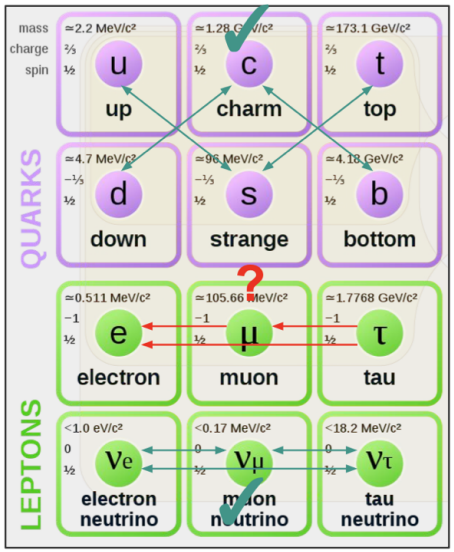

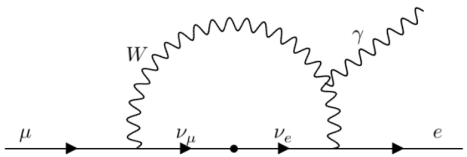

Charged Lepton Flavour Violation (CLFV)

- Flavor is not conserved in:
  1. Quarks (quark mixing, CKM matrix)
  2. Neutrinos (neutrino oscillations, PMNS matrix)
  3. Charged leptons ?

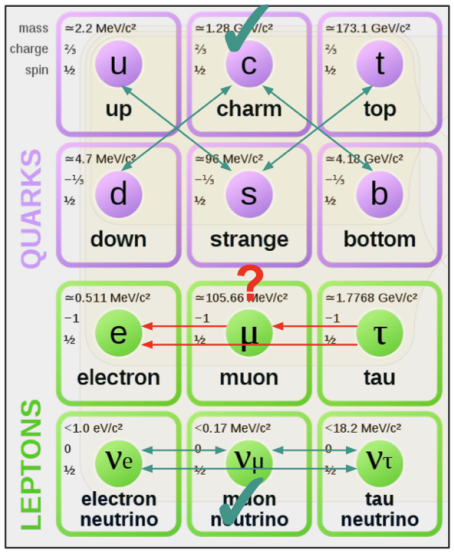

- CLFV processes can occur through neutrino oscillation.

$$BR(\mu \to e\gamma) = \frac{3\alpha}{32\pi}(\frac{1}{4})sin^2 2\theta_{13} sin^2\theta_{23} |\frac{\Delta m^2_{13}}{M^2_W}|^2$$

- BR of CLFV processes through neutrino oscillations are suppressed by factors proportional to $(\Delta m^2_\nu)^2/M^4_W$ to undetectably tiny levels, $< 10^{-50}$.

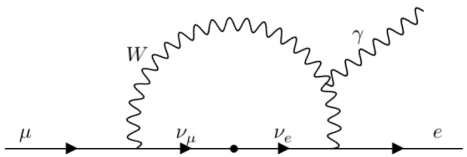

Observation of CLFV process would be unambiguous evidence of New Physics

BSM models

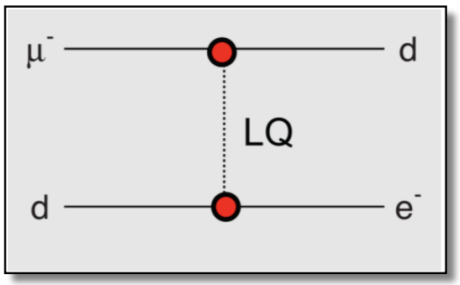

Leptoquarks

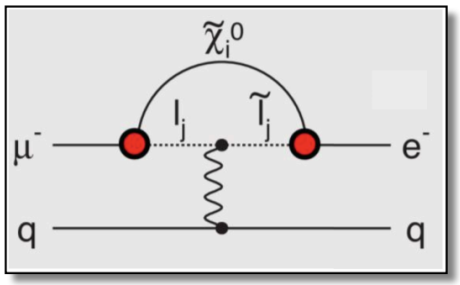

Supersymmetry

Pictures adapted from W. Marciano

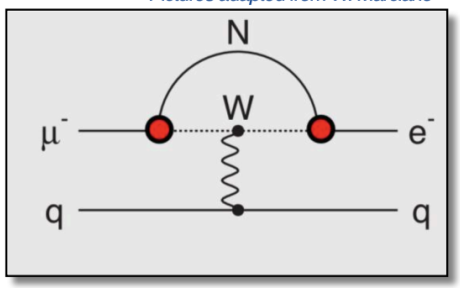

Heavy neutrinos

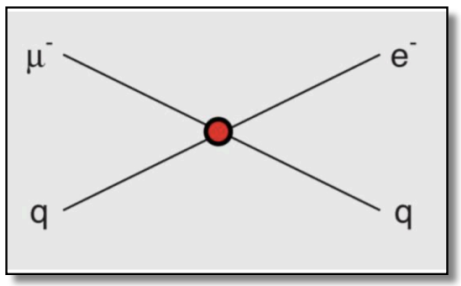

Compositeness

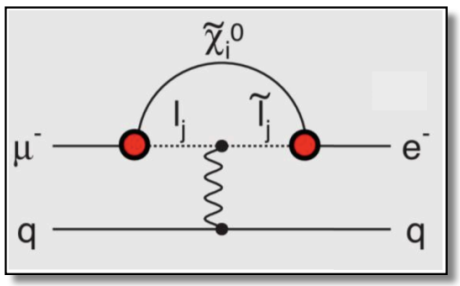

Second Higgs doublet

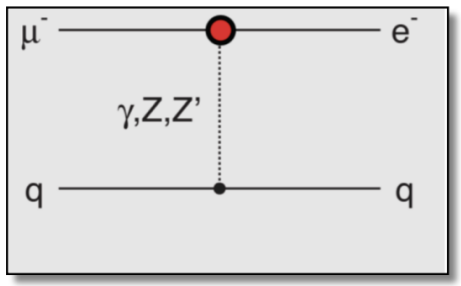

Anomal Z couple

Most BSM theories predict CLFV processes with B.R. much higher than the SM predictions, up to the order of less than 10^{-15}, and are within the sensitivity of next-generation experiments.

Model independent $\mathcal{L}$ for CLFV

A model independent effective Lagrangian involving muons [1]:

$$\mathcal{L}_{CLFV} = \frac{m_\mu}{(1+\kappa)\Lambda^2}\bar{\mu}_R\sigma_{\mu\nu}e_L F^{\mu\nu} + \frac{\kappa}{(1+\kappa)\Lambda^2}\bar{\mu}_L\gamma_\mu e_L \sum_{q=u,d}\bar{q}_L\gamma^\mu q_L$$

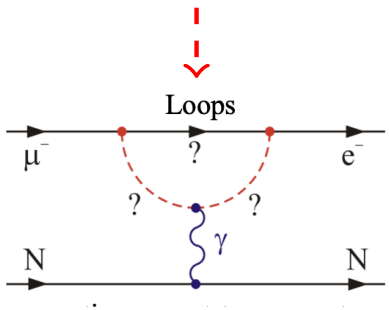

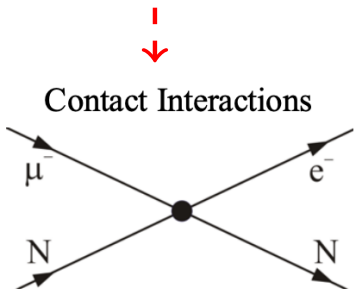

Model independent $\mathcal{L}$ for CLFV

A model independent effective Lagrangian involving muons [1]:

$$\mathcal{L}_{CLFV} = \frac{m_\mu}{(1+\kappa)\Lambda^2}\bar{\mu}_R\sigma_{\mu\nu}e_L F^{\mu\nu} + \frac{\kappa}{(1+\kappa)\Lambda^2}\bar{\mu}_L\gamma_\mu e_L \sum_{q=u,d}\bar{q}_L\gamma^\mu q_L$$

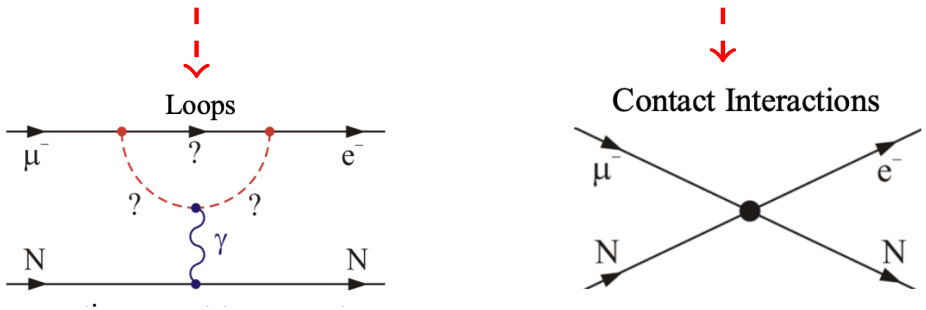

- Λ is the effective mass scale and κ controls the relative contribution of the dipole interaction term and the four fermion term.

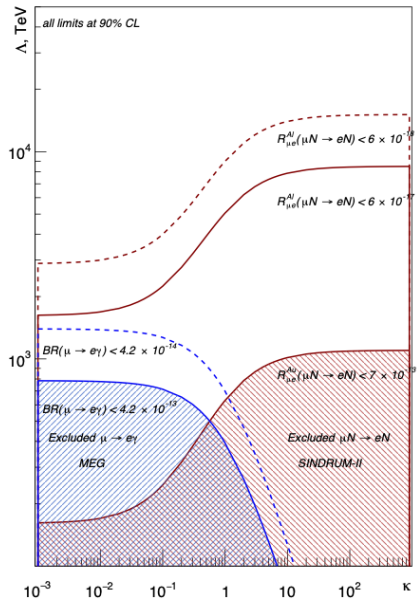

Model independent $\mathcal{L}$ for CLFV

A model independent effective Lagrangian involving muons [1]:

$$\mathcal{L}_{CLFV} = \frac{m_\mu}{(1+\kappa)\Lambda^2}\bar{\mu}_R\sigma_{\mu\nu}e_L F^{\mu\nu} + \frac{\kappa}{(1+\kappa)\Lambda^2}\bar{\mu}_L\gamma_\mu e_L \sum_{q=u,d}\bar{q}_L\gamma^\mu q_L$$

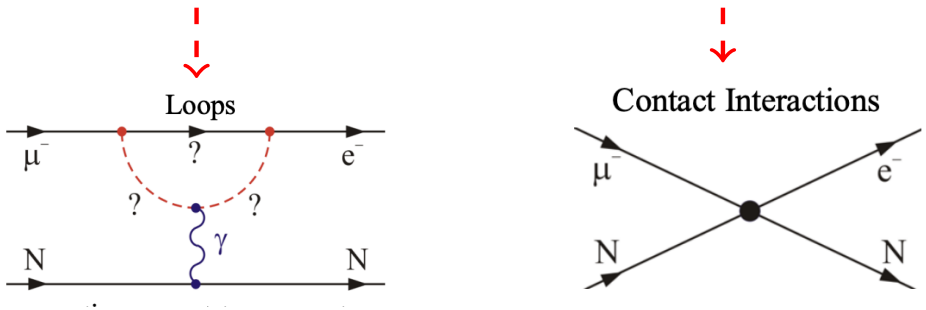

- Λ is the effective mass scale and κ controls the relative contribution of the dipole interaction term and the four fermion term.
- $\kappa \ll 1$, dipole interaction term dominates, mediates $\mu \to e\gamma$ directly, $\mu N \to eN$ at order α.

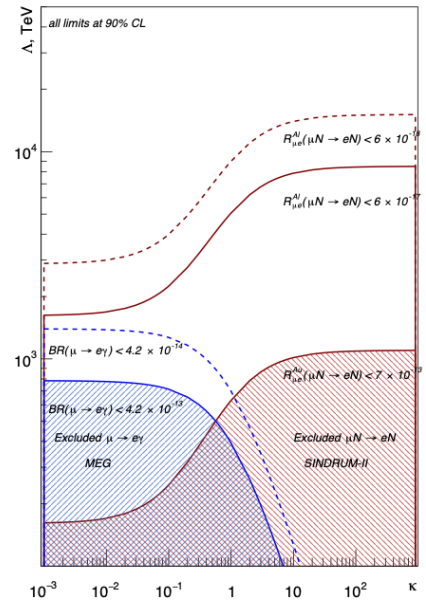

Model independent $\mathcal{L}$ for CLFV

A model independent effective Lagrangian involving muons [1]:

$$\mathcal{L}_{CLFV} = \frac{m_\mu}{(1+\kappa)\Lambda^2}\bar{\mu}_R\sigma_{\mu\nu}e_L F^{\mu\nu} + \frac{\kappa}{(1+\kappa)\Lambda^2}\bar{\mu}_L\gamma_\mu e_L \sum_{q=u,d}\bar{q}_L\gamma^\mu q_L$$

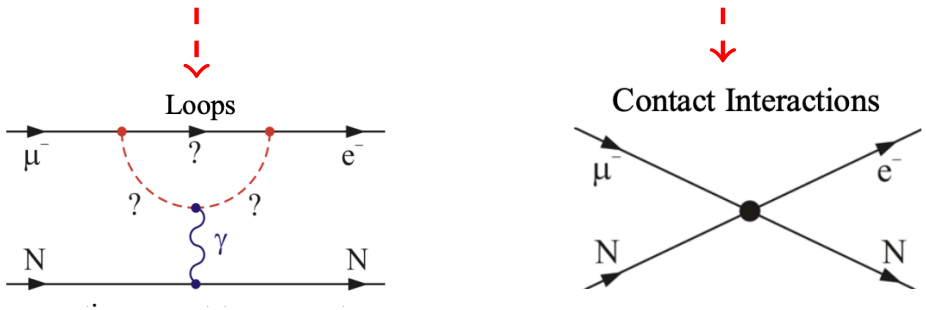

- Λ is the effective mass scale and κ controls the relative contribution of the dipole interaction term and the four fermion term.
- $\kappa \ll 1$, dipole interaction term dominates, mediates $\mu \to e\gamma$ directly, $\mu N \to eN$ at order α.
- $\kappa \gg 1$, the four fermion contact term dominates, mediates $\mu N \to eN$ at LO and $\mu \to e\gamma$ at loop level.

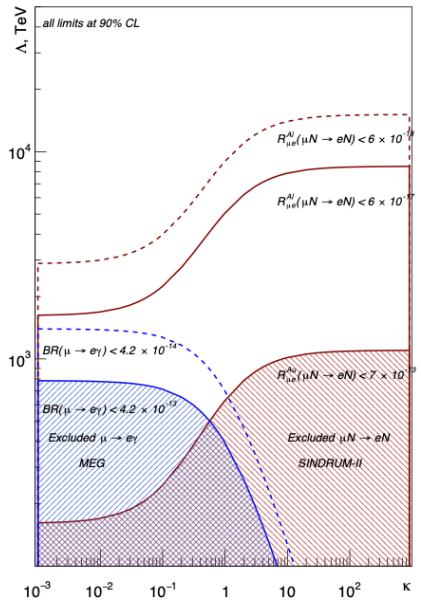

Muon CLFV channels

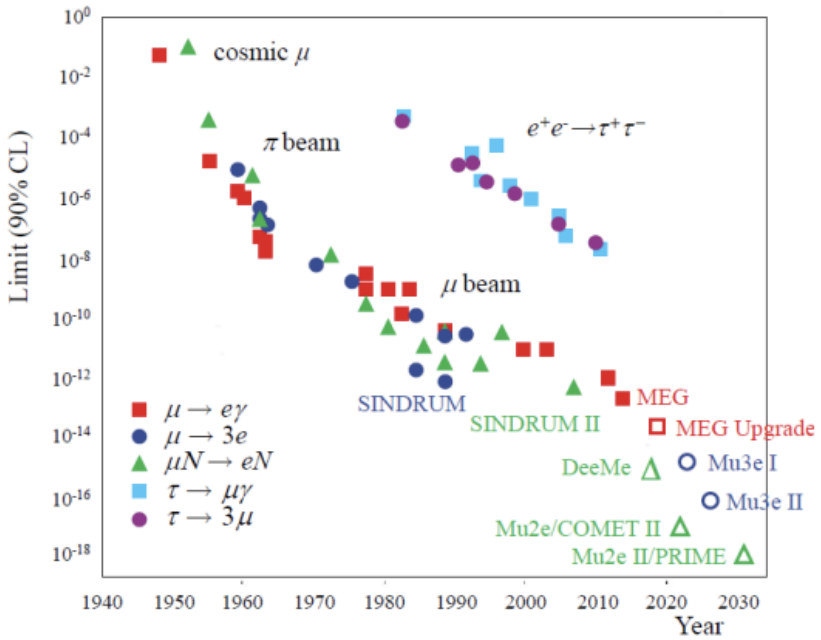

Muon CLFV channels

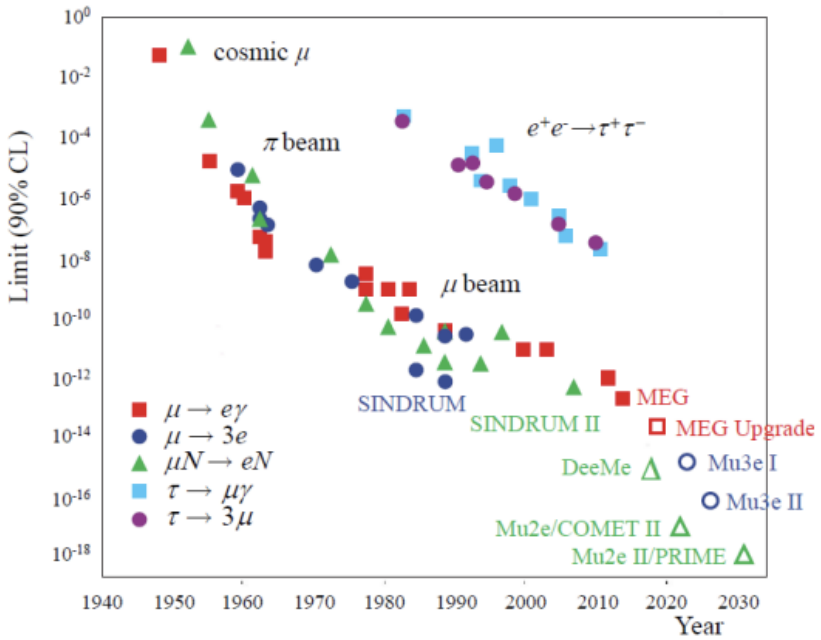

- Muons are among the most promising candidates for CLFV searches:

Muon CLFV channels

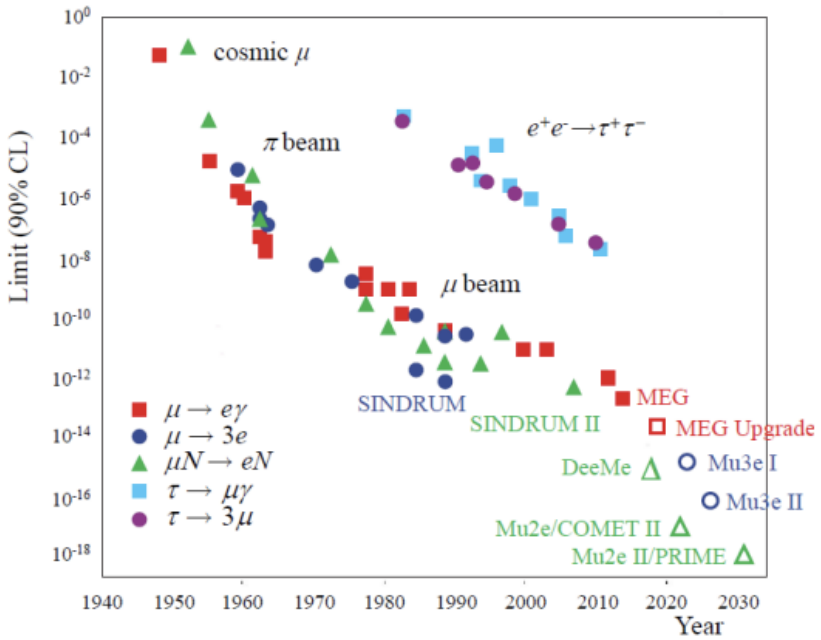

- Muons are among the most promising candidates for CLFV searches:
  1. Easy to produce (from pion and kaon decays).

Muon CLFV channels

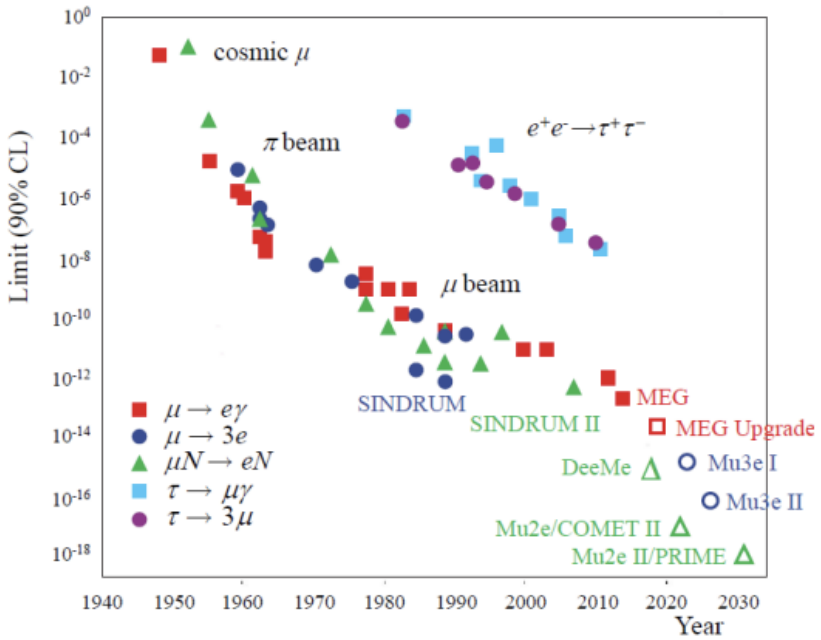

- Muons are among the most promising candidates for CLFV searches:
  1. Easy to produce (from pion and kaon decays).
  2. Muon lifetime ($\tau_\mu \sim 2.2\mu$s) is much longer than tau lifetime ($\tau_\tau \sim 0.29$ ps), enabling the formation of high intensity muon beams.

Muon CLFV channels

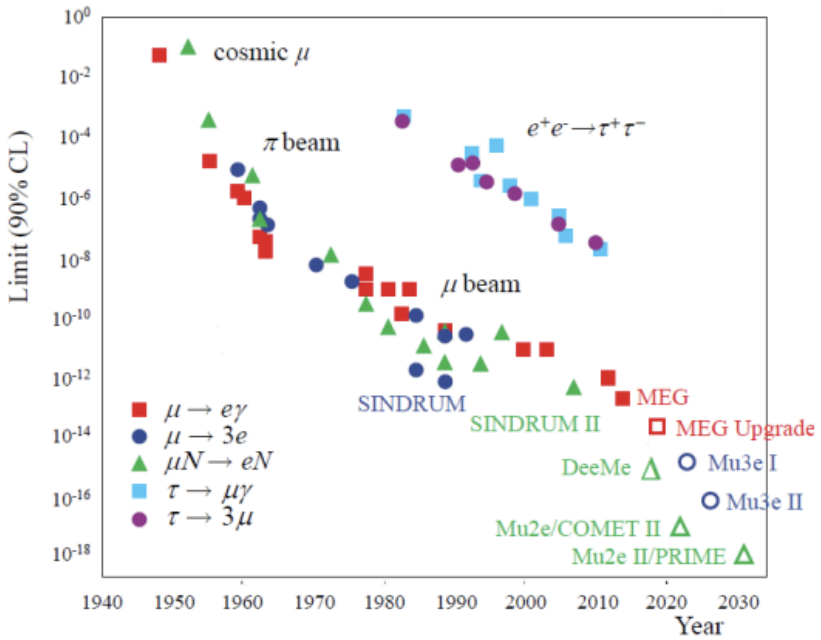

- Muons are among the most promising candidates for CLFV searches:
  1. Easy to produce (from pion and kaon decays).
  2. Muon lifetime ($\tau_\mu \sim 2.2\mu$s) is much longer than tau lifetime ($\tau_\tau \sim 0.29$ ps), enabling the formation of high intensity muon beams.
- Golden channels: $\mu^+ \to e^+\gamma$ $\quad$ $\mu^+ \to e^+e^-e^+$

Muon CLFV channels

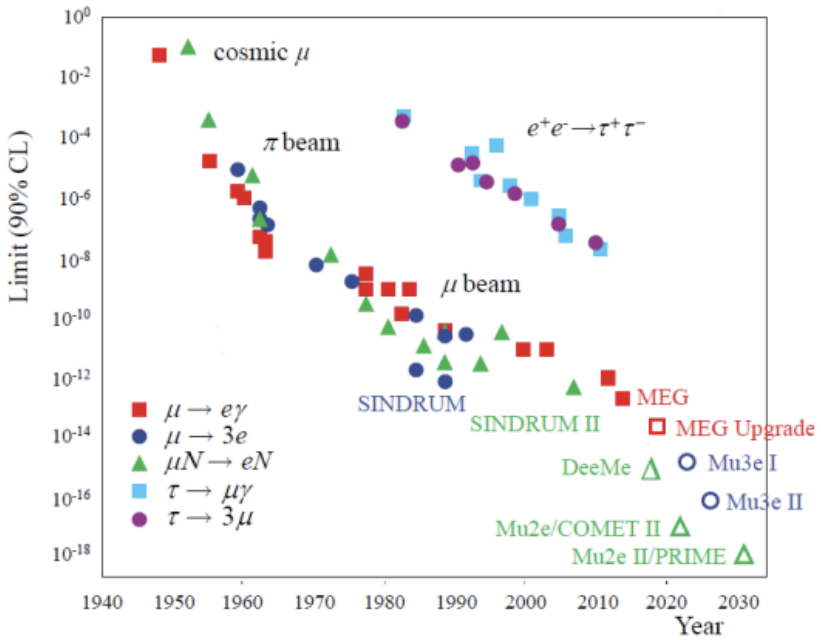

- Muons are among the most promising candidates for CLFV searches:
  1. Easy to produce (from pion and kaon decays).
  2. Muon lifetime ($\tau_\mu \sim 2.2\mu$s) is much longer than tau lifetime ($\tau_\tau \sim 0.29$ ps), enabling the formation of high intensity muon beams.
- Golden channels: $\mu^+ \to e^+\gamma$ $\mu^+ \to e^+e^-e^+$ $\boxed{\mu^- N \to e^- N}$

$\mu^- N \to e^- N$

- Search for neutrinoless, coherent conversion of muon to electron in the field of a nucleus by measuring,

$$R_{\mu e} = \frac{\Gamma(\mu^- + N(Z,A) \to e^- + N(Z,A))}{\Gamma(\mu^- + N(Z,A) \to \nu_\mu + N(Z-1,A))}$$

For Al target, signal is a $\sim$105 MeV e^-.

$\mu^- N \to e^- N$

- Search for neutrinoless, coherent conversion of muon to electron in the field of a nucleus by measuring,

$$R_{\mu e} = \frac{\Gamma(\mu^- + N(Z,A) \to e^- + N(Z,A))}{\Gamma(\mu^- + N(Z,A) \to \nu_\mu + N(Z-1,A))}$$

  For Al target, signal is a $\sim$105 MeV e^-.

- Advantages of this channel:

$\mu^- N \to e^- N$

- Search for neutrinoless, coherent conversion of muon to electron in the field of a nucleus by measuring,

$$R_{\mu e} = \frac{\Gamma(\mu^- + N(Z,A) \to e^- + N(Z,A))}{\Gamma(\mu^- + N(Z,A) \to \nu_\mu + N(Z-1,A))}$$

For Al target, signal is a $\sim$105 MeV e^-.

- Advantages of this channel:
  1. Almost no combinatorial background.

$\mu^- N \to e^- N$

- Search for neutrinoless, coherent conversion of muon to electron in the field of a nucleus by measuring,

$$R_{\mu e} = \frac{\Gamma(\mu^- + N(Z,A) \to e^- + N(Z,A))}{\Gamma(\mu^- + N(Z,A) \to \nu_\mu + N(Z-1,A))}$$

For Al target, signal is a $\sim$105 MeV e^-.

- Advantages of this channel:
  1. Almost no combinatorial background.
  2. Best sensitivity to a large range of NP scenarios.

$\mu^- N \to e^- N$

- Search for neutrinoless, coherent conversion of muon to electron in the field of a nucleus by measuring,

$$R_{\mu e} = \frac{\Gamma(\mu^- + N(Z,A) \to e^- + N(Z,A))}{\Gamma(\mu^- + N(Z,A) \to \nu_\mu + N(Z-1,A))}$$

For Al target, signal is a ∼105 MeV e^-.

- Advantages of this channel:
  1. Almost no combinatorial background.
  2. Best sensitivity to a large range of NP scenarios.
  3. Can give unique information regarding underlying NP operators.

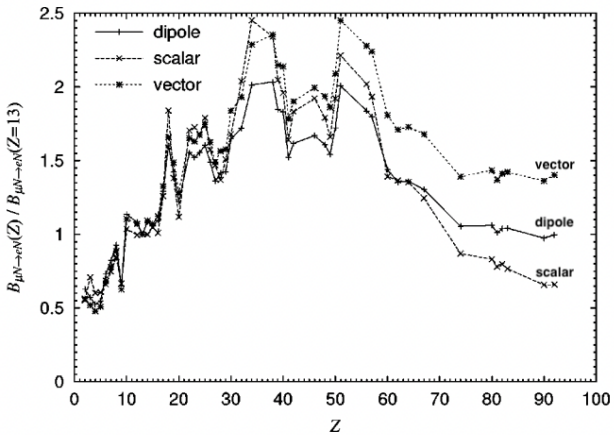

$\mu^- \to e^-$ conversion ratio plotted as a function of atomic number, Z. The conversion ratios are normalized by the conversion ratio in aluminum nucleus ($Z_{Al} = 13$) [2].

$\mu^- N \to e^- N$

- Search for neutrinoless, coherent conversion of muon to electron in the field of a nucleus by measuring,

$$R_{\mu e} = \frac{\Gamma(\mu^- + N(Z,A) \to e^- + N(Z,A))}{\Gamma(\mu^- + N(Z,A) \to \nu_\mu + N(Z-1,A))}$$

For Al target, signal is a $\sim$105 MeV e^-.

- Advantages of this channel:
  1. Almost no combinatorial background.
  2. Best sensitivity to a large range of NP scenarios.
  3. Can give unique information regarding underlying NP operators.
- Current best limit set by SINDRUM II experiment $R_{\mu e} < 7 \times 10^{-13}$ (90% C.L).

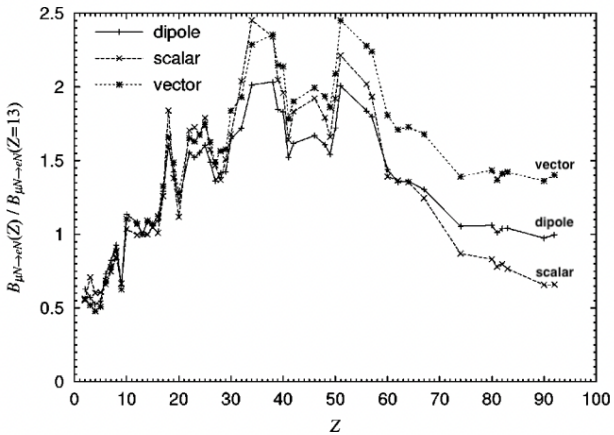

$\mu^- \to e^-$ conversion ratio plotted as a function of atomic number, Z. The conversion ratios are normalized by the conversion ratio in aluminum nucleus ($Z_{Al} = 13$) [2].

Mu2e experiment

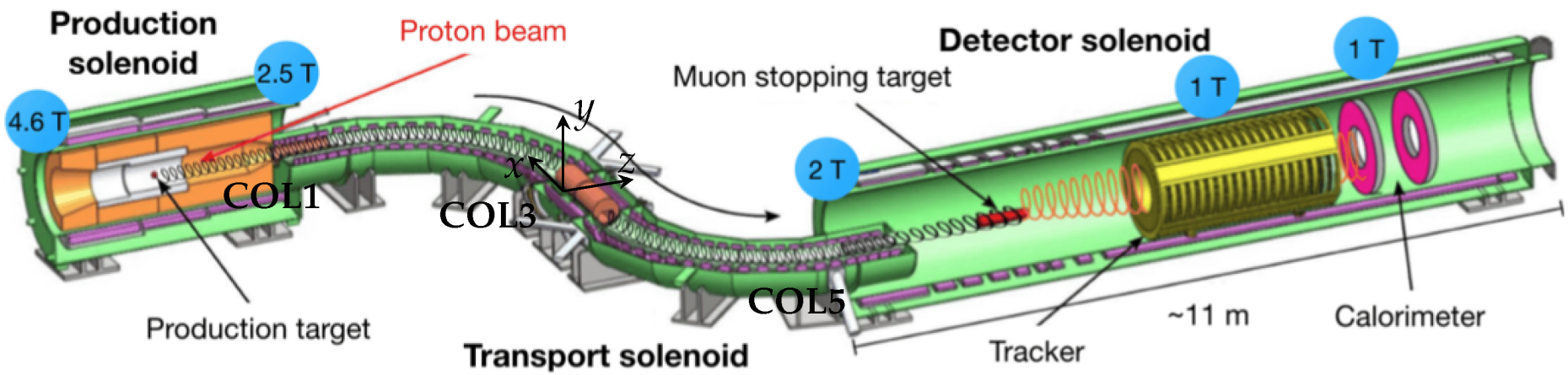

Mu2e experiment

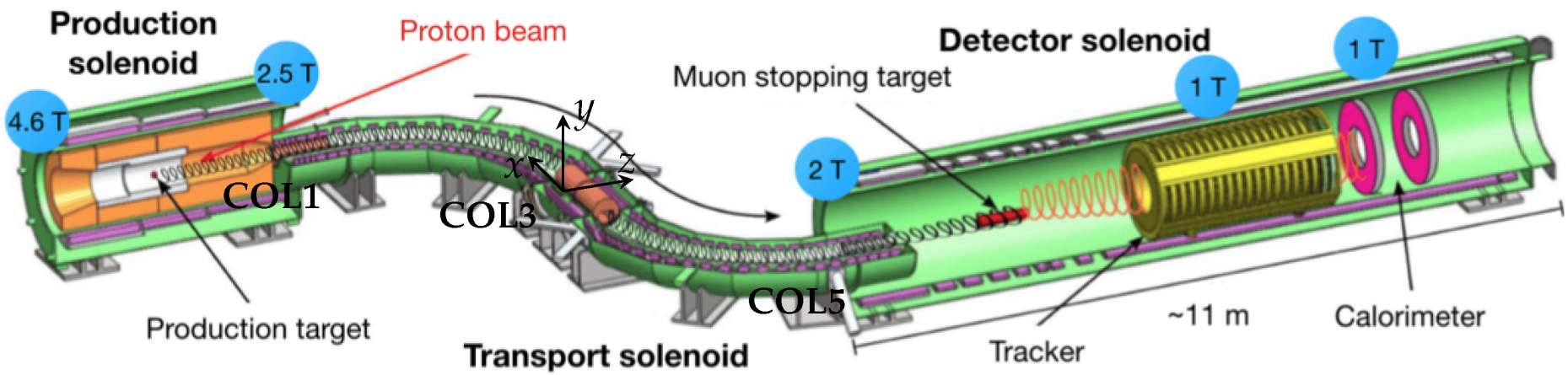

PS

8 GeV pulsed proton beam interacts with the production target, mostly produces pions. Pions decay into muons.

Mu2e experiment

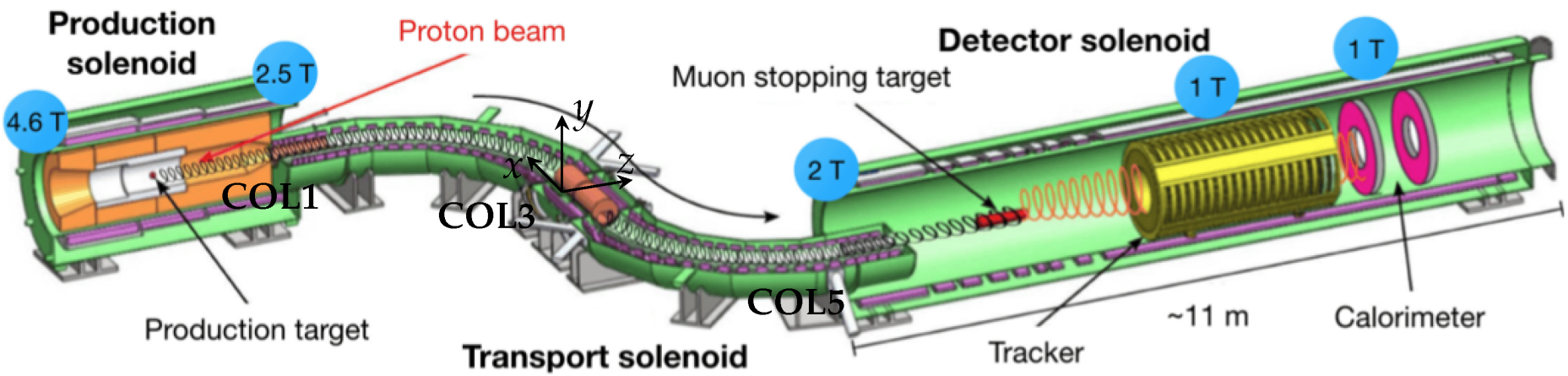

PS

8 GeV pulsed proton beam interacts with the production target, mostly produces pions. Pions decay into muons.

TS

S-shaped. Selects low-momentum muons and pions. Rotating collimator COL3 selects μ^-/μ^+ beam.

Mu2e experiment

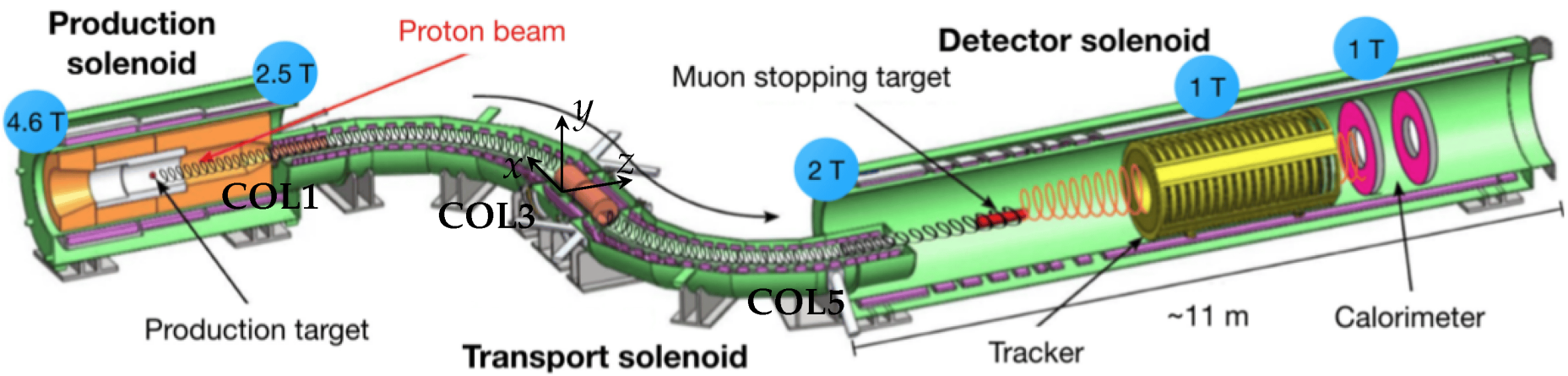

PS

8 GeV pulsed proton beam interacts with the production target, mostly produces pions. Pions decay into muons.

TS

S-shaped. Selects low-momentum muons and pions. Rotating collimator COL3 selects μ^-/μ^+ beam.

DS

Muons stop in the Al stopping target. Annular tracker and calorimeter to detect potential conversion e^- (CE).

Signal and Backgrounds

Signal

- Signal: Monochromatic conversion electron (CE) with energy,

$$E_{CE} = m_{\mu} - E_{bind} - E_{recoil}$$

where E_{bind} is the binding energy of 1s state of the muonic atom, E_{recoil} is the recoil energy of the target nucleus.

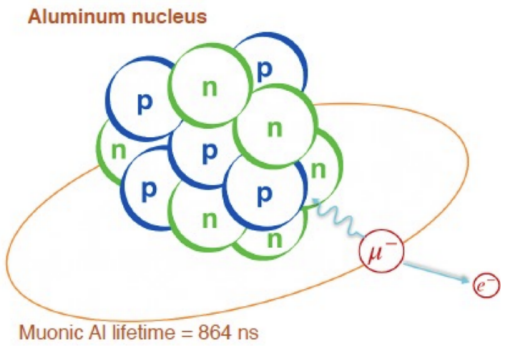

Signal

- Signal: Monochromatic conversion electron (CE) with energy,

$$E_{CE} = m_{\mu} - E_{bind} - E_{recoil}$$

where E_{bind} is the binding energy of 1s state of the muonic atom, E_{recoil} is the recoil energy of the target nucleus.

- For Al target, $E_{CE} = 104.97$ MeV.

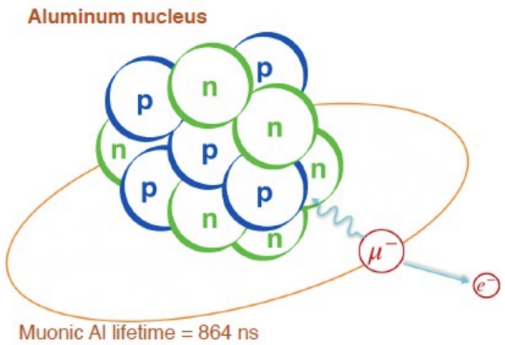

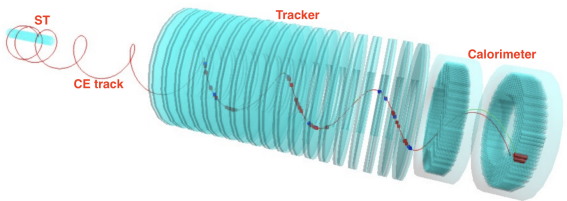

Signal

- Signal: Monochromatic conversion electron (CE) with energy,

$$E_{CE} = m_{\mu} - E_{bind} - E_{recoil}$$

where E_{bind} is the binding energy of 1s state of the muonic atom, E_{recoil} is the recoil energy of the target nucleus.

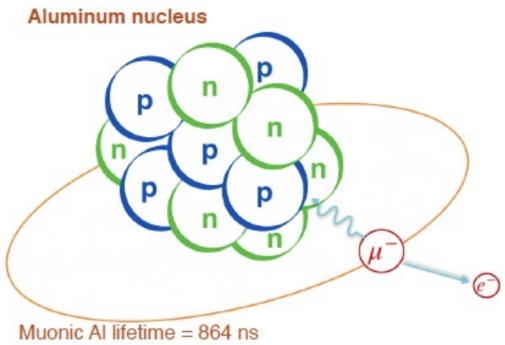

- For Al target, $E_{CE} = 104.97$ MeV.
- The lifetime of the muonic aluminum atom is ~864 ns. Muons can undergo,

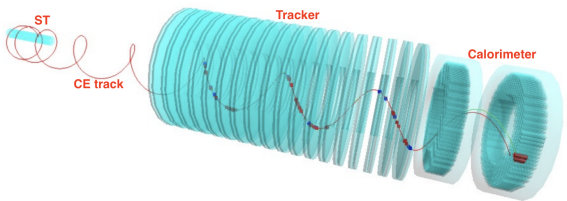

Signal

- Signal: Monochromatic conversion electron (CE) with energy,

$$E_{CE} = m_{\mu} - E_{bind} - E_{recoil}$$

where E_{bind} is the binding energy of 1s state of the muonic atom, E_{recoil} is the recoil energy of the target nucleus.

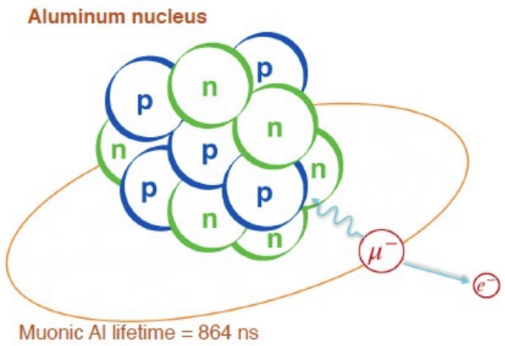

- For Al target, $E_{CE} = 104.97$ MeV.
- The lifetime of the muonic aluminum atom is ~864 ns. Muons can undergo,
  1. Nuclear muon capture (~61%): $\mu^- + {}^{27}_{13}Al \rightarrow \nu_{\mu} + {}^{27}_{13}Mg^*$

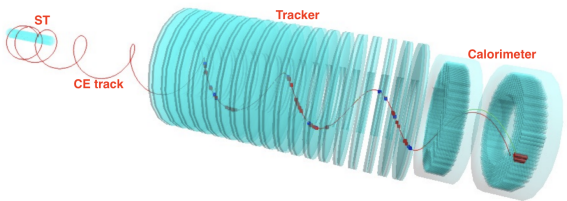

Signal

- Signal: Monochromatic conversion electron (CE) with energy,

$$E_{CE} = m_{\mu} - E_{bind} - E_{recoil}$$

where E_{bind} is the binding energy of 1s state of the muonic atom, E_{recoil} is the recoil energy of the target nucleus.

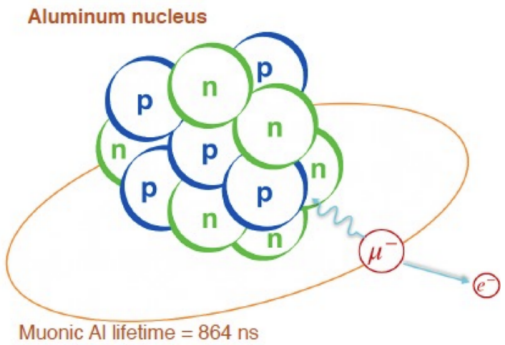

- For Al target, $E_{CE} = 104.97$ MeV.
- The lifetime of the muonic aluminum atom is ~864 ns. Muons can undergo,
  1. Nuclear muon capture (~61%): $\mu^- + {}^{27}_{13}Al \rightarrow \nu_{\mu} + {}^{27}_{13}Mg^*$ (Normalizing factor in $R_{\mu e}$)

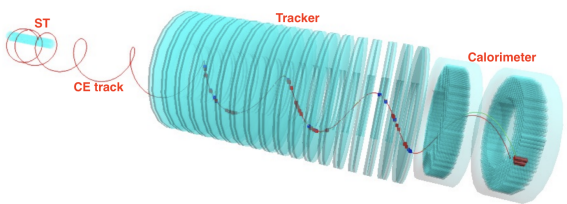

Signal

- Signal: Monochromatic conversion electron (CE) with energy,

$$E_{CE} = m_{\mu} - E_{bind} - E_{recoil}$$

where E_{bind} is the binding energy of 1s state of the muonic atom, E_{recoil} is the recoil energy of the target nucleus.

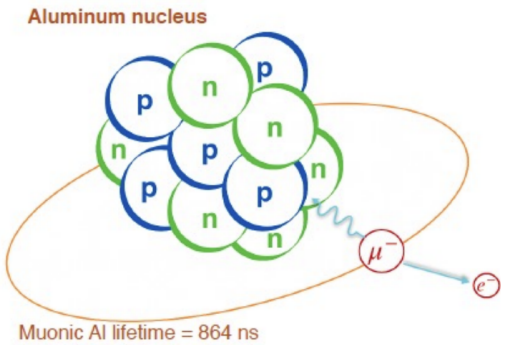

- For Al target, $E_{CE} = 104.97$ MeV.
- The lifetime of the muonic aluminum atom is ~864 ns. Muons can undergo,
  1. Nuclear muon capture (~61%):
     $\mu^- + {}^{27}_{13}Al \rightarrow \nu_{\mu} + {}^{27}_{13}Mg^*$
     (Normalizing factor in $R_{\mu e}$)
  2. Muon decay in orbit (~ 39%):
     $\mu^- + {}^{27}_{13}Al \rightarrow e^- + \bar{\nu}_e + \nu_{\mu} + {}^{27}_{13}Al$

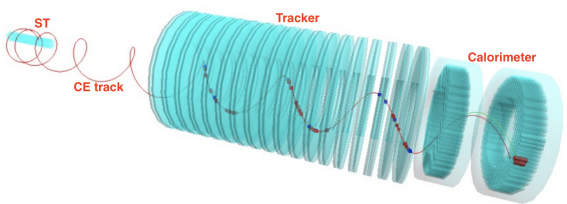

Signal

- Signal: Monochromatic conversion electron (CE) with energy,

$$E_{CE} = m_{\mu} - E_{bind} - E_{recoil}$$

where E_{bind} is the binding energy of 1s state of the muonic atom, E_{recoil} is the recoil energy of the target nucleus.

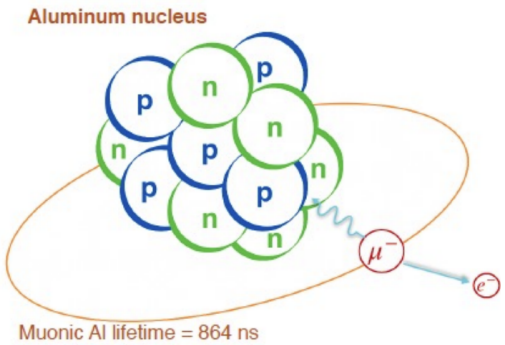

- For Al target, $E_{CE} = 104.97$ MeV.
- The lifetime of the muonic aluminum atom is ~864 ns. Muons can undergo,
  1. Nuclear muon capture (~61%):
     $\mu^- + {}^{27}_{13}Al \rightarrow \nu_{\mu} + {}^{27}_{13}Mg^*$
     (Normalizing factor in $R_{\mu e}$)
  2. Muon decay in orbit (~ 39%):
     $\mu^- + {}^{27}_{13}Al \rightarrow e^- + \bar{\nu}_e + \nu_{\mu} + {}^{27}_{13}Al$
     (Potential background)

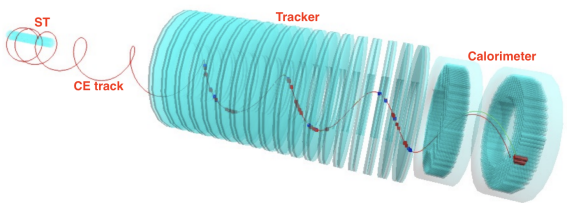

Background

1. Decay in orbit (DIO) : Free μ^- decay follows the Michel spectrum with e^- kinematic endpoint at $m_\mu/2$. In the field of a nucleus, the endpoint extends to the CE energy [3].

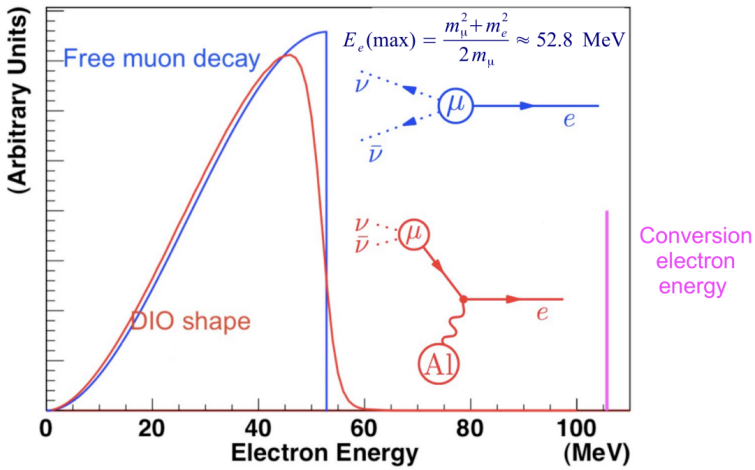

Background

1. Decay in orbit (DIO) : Free μ^- decay follows the Michel spectrum with e^- kinematic endpoint at $m_\mu/2$. In the field of a nucleus, the endpoint extends to the CE energy [3].
   Use a straw tracker with good momentum resolution.

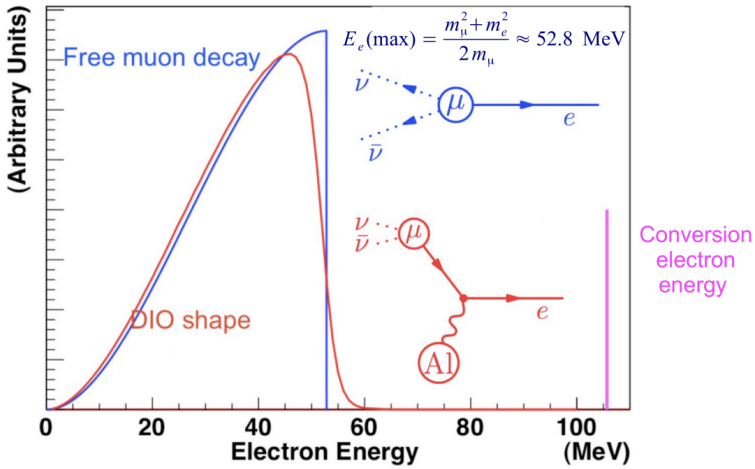

Background

1. Decay in orbit (DIO) : Free μ^- decay follows the Michel spectrum with e^- kinematic endpoint at $m_\mu/2$. In the field of a nucleus, the endpoint extends to the CE energy [3].
   Use a straw tracker with good momentum resolution.
2. Cosmic Rays: Cosmic muons interacting or decaying within the detector are expected to produce ∼1 CE like event per day.

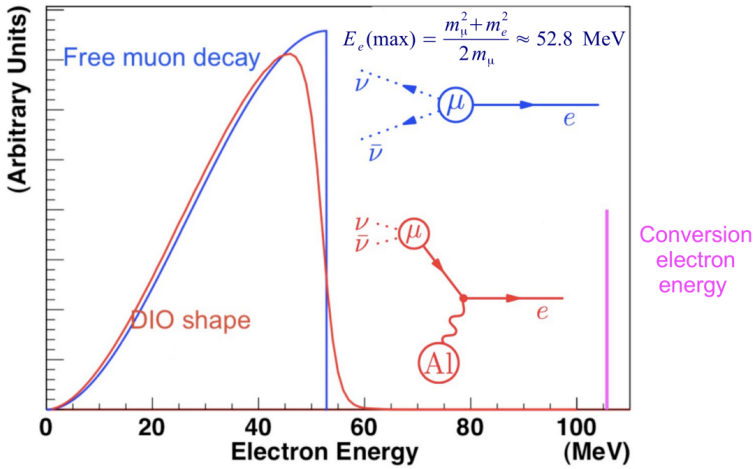

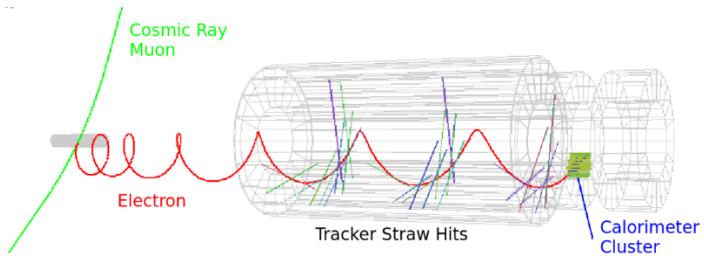

Background

1. Decay in orbit (DIO) : Free μ^- decay follows the Michel spectrum with e^- kinematic endpoint at $m_\mu/2$. In the field of a nucleus, the endpoint extends to the CE energy [3].
   Use a straw tracker with good momentum resolution.

2. Cosmic Rays: Cosmic muons interacting or decaying within the detector are expected to produce ∼1 CE like event per day.
   A cosmic ray veto system built from scintillator counters surrounds the detector solenoid.

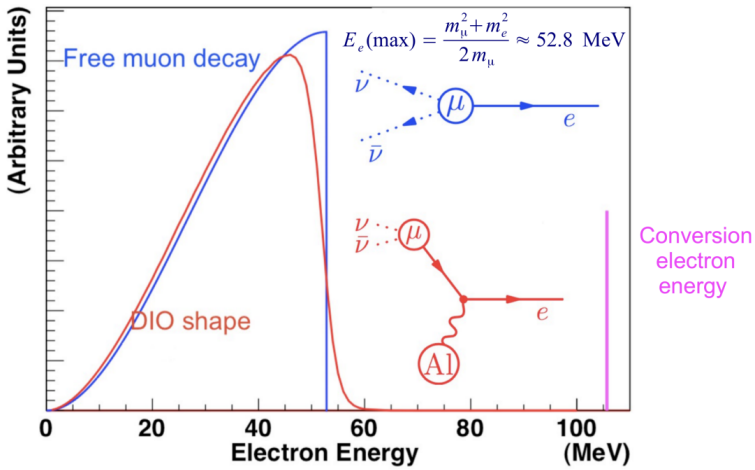

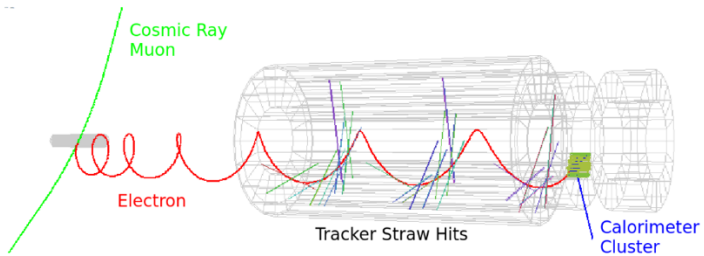

Backgrounds

3. Radiative Pion Capture (RPC):
   $\pi^- + N(A, Z) \rightarrow \gamma^{(*)}(e^+e^-) + N(A, Z-1)$

Backgrounds

3. Radiative Pion Capture (RPC):
$\pi^- + N(A,Z) \to \gamma^{(*)}(e^+e^-) + N(A,Z-1)$ Due to short lifetime of pions, this background can be suppressed by using pulsed proton beam along with a delayed live-time window.

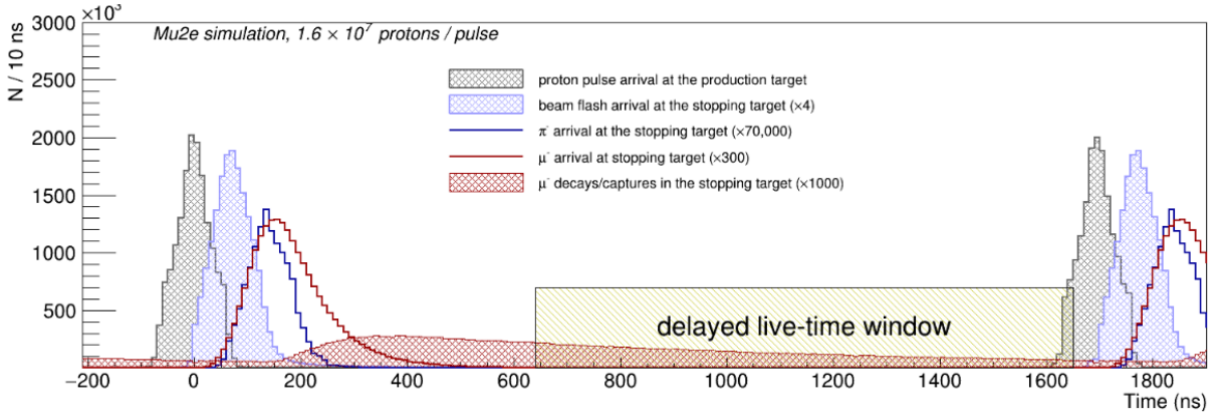

Backgrounds

3. Radiative Pion Capture (RPC):
   $\pi^- + N(A,Z) \to \gamma^{(*)}(e^+e^-) + N(A,Z-1)$ Due to short lifetime of pions, this background can be suppressed by using pulsed proton beam along with a delayed live-time window.

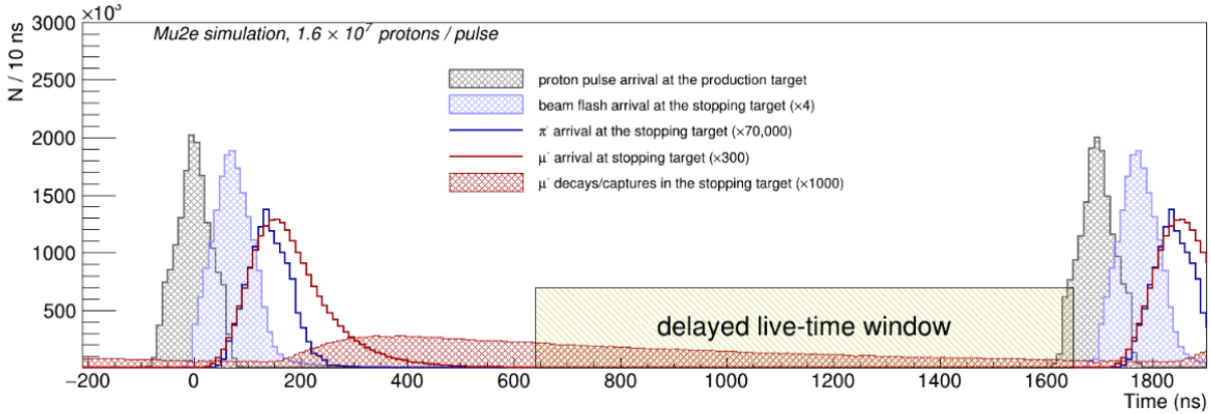

4. Radiative Muon Capture: $\mu^- + N(A,Z) \to \gamma^{(*)} + \nu_\mu + N(A,Z-1)$

Backgrounds

3. Radiative Pion Capture (RPC):
$\pi^- + N(A,Z) \to \gamma^{(*)}(e^+e^-) + N(A,Z-1)$ Due to short lifetime of pions, this background can be suppressed by using pulsed proton beam along with a delayed live-time window.

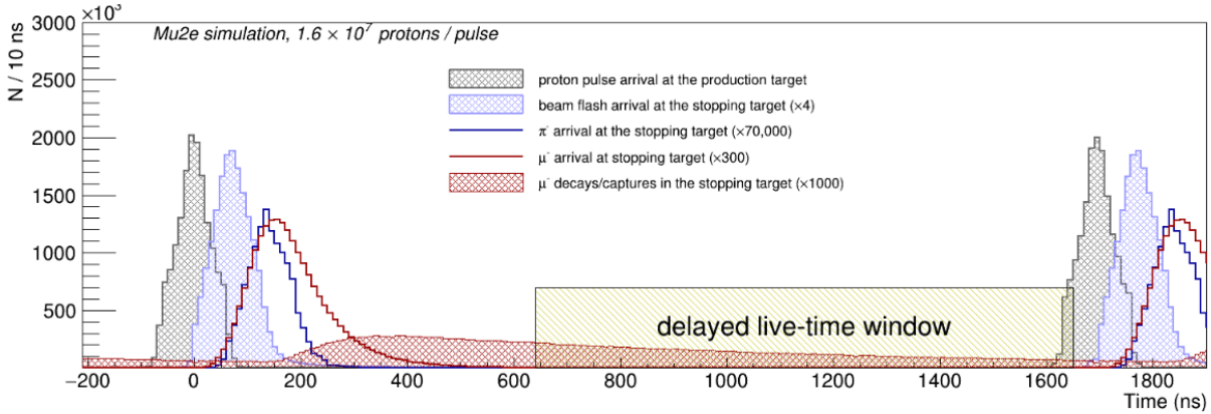

4. Radiative Muon Capture: $\mu^- + N(A,Z) \to \gamma^{(*)} + \nu_\mu + N(A,Z-1)$ Analogous to RPC, but with lower maximal energy. In Al it is $\sim$102 MeV.

Backgrounds

3. Radiative Pion Capture (RPC):
$\pi^- + N(A,Z) \to \gamma^{(*)}(e^+e^-) + N(A,Z-1)$ Due to short lifetime of pions, this background can be suppressed by using pulsed proton beam along with a delayed live-time window.

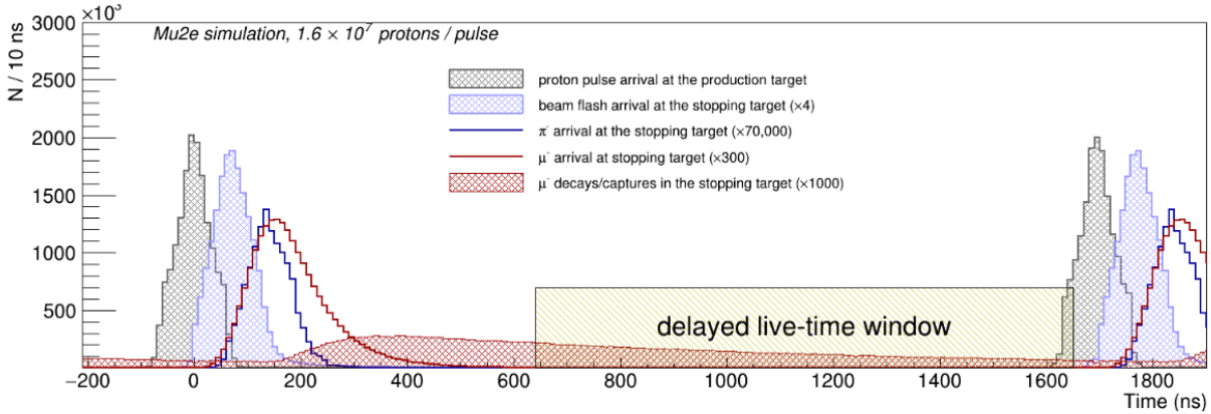

4. Radiative Muon Capture: $\mu^- + N(A,Z) \to \gamma^{(*)} + \nu_\mu + N(A,Z-1)$ Analogous to RPC, but with lower maximal energy. In Al it is $\sim$102 MeV.

5. Antiprotons: Produced in the proton beam interactions with production target, can reach the stopping target and annihilate to produce signal-like e^-.

Backgrounds

3. Radiative Pion Capture (RPC):
$\pi^- + N(A,Z) \to \gamma^{(*)}(e^+e^-) + N(A,Z-1)$ Due to short lifetime of pions, this background can be suppressed by using pulsed proton beam along with a delayed live-time window.

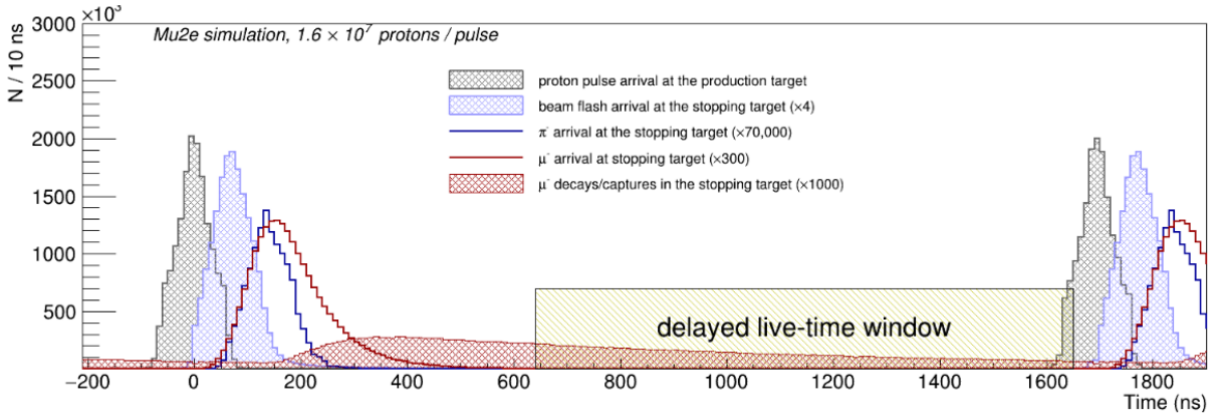

4. Radiative Muon Capture: $\mu^- + N(A,Z) \to \gamma^{(*)} + \nu_\mu + N(A,Z-1)$ Analogous to RPC, but with lower maximal energy. In Al it is $\sim$102 MeV.

5. Antiprotons: Produced in the proton beam interactions with production target, can reach the stopping target and annihilate to produce signal-like e^-. Absorber elements placed at entrance and center of the Transport Solenoid.

Run I Sensitivity

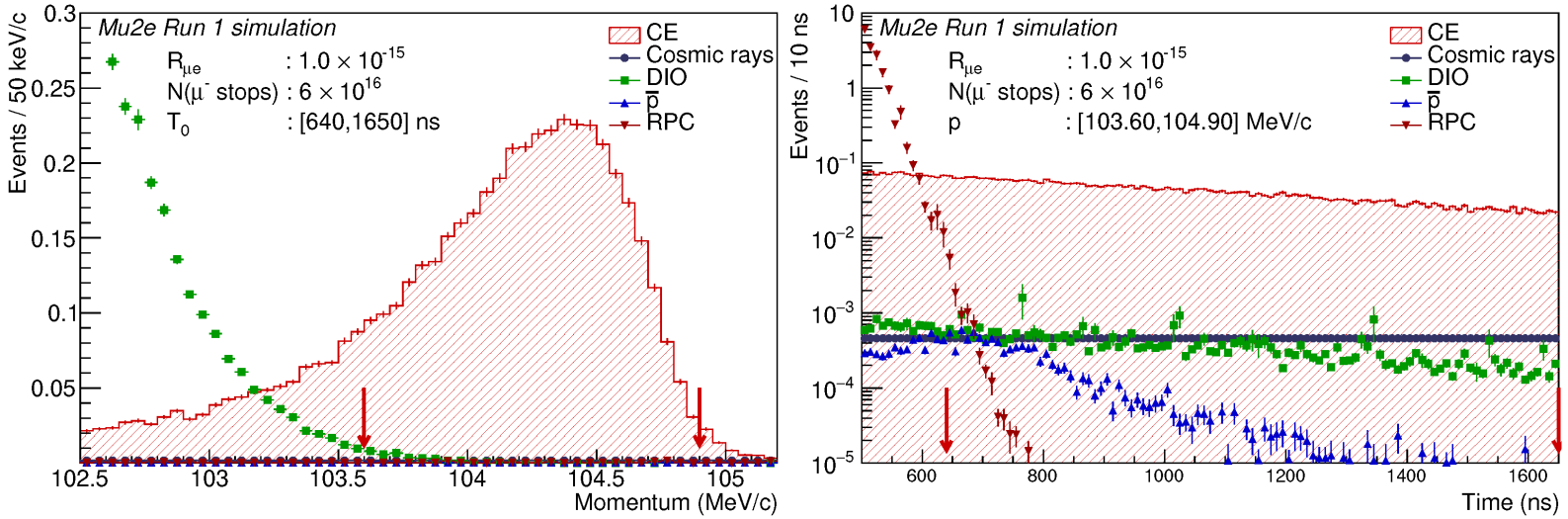

Left: Momentum distribution of the CE signal and expected backgrounds.
Right: Time distribution of the CE signal and expected backgrounds.
Signal region selected for analysis, $103.60 < p < 104.90$ MeV/c and $640 < T0 < 1650$ ns.

- Mu2e Run I assumes an integrated flux of 6×10^{16} stopped muons.
- The expected Run I 5σ discovery sensitivity is $R_{\mu e} = 1.2 \times 10^{-15}$, with a total expected background of 0.11 ± 0.03 events.

Run I Sensitivity

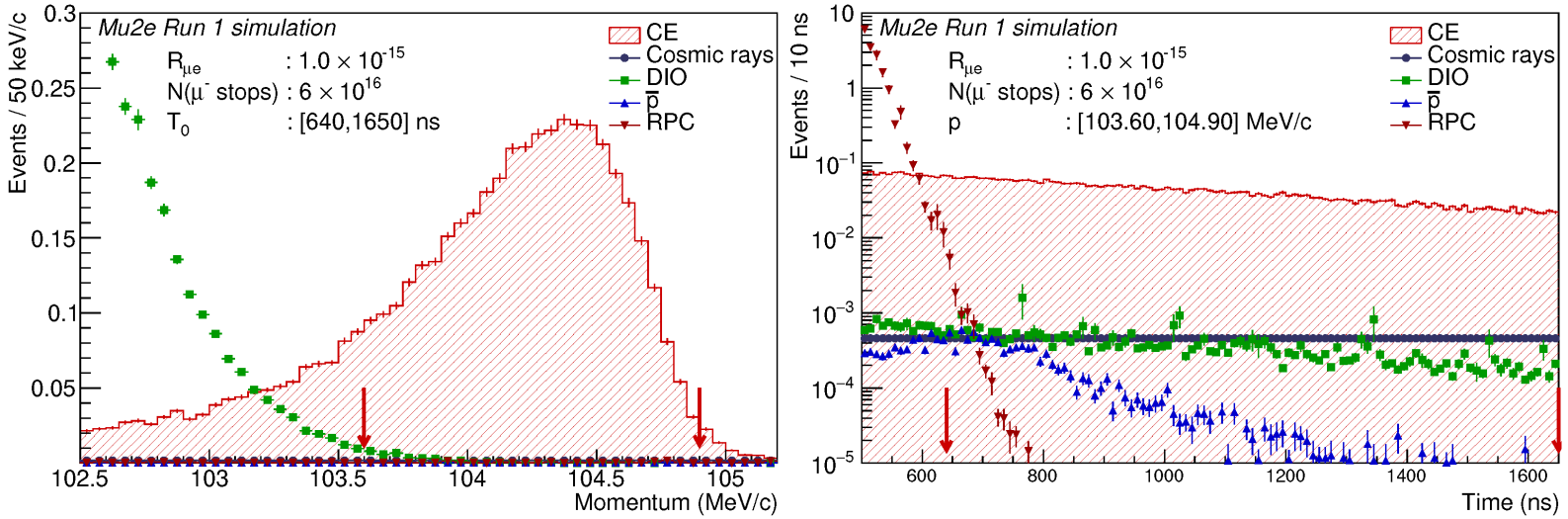

Left: Momentum distribution of the CE signal and expected backgrounds.
Right: Time distribution of the CE signal and expected backgrounds.
Signal region selected for analysis, $103.60 < p < 104.90$ MeV/c and $640 < T0 < 1650$ ns.

- Mu2e Run I assumes an integrated flux of 6×10^{16} stopped muons.
- The expected Run I 5σ discovery sensitivity is $R_{\mu e} = 1.2 \times 10^{-15}$, with a total expected background of 0.11 ± 0.03 events.
- In the absence of a signal, the expected upper limit is $R_{\mu e} < 6.2 \times 10^{-16}$ at 90% C.L [4].

Mu2e Detectors

Straw tube Tracker

- Annular geometry to reject most of DIO electron tracks.

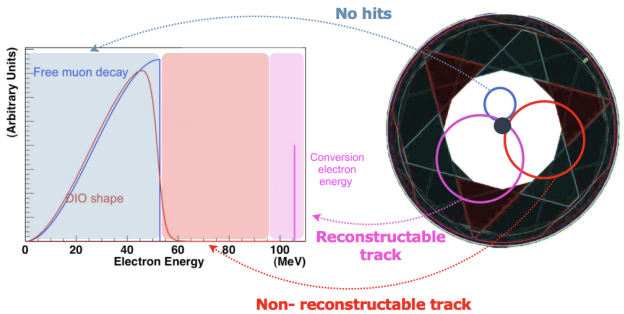

Straw tube Tracker

- Annular geometry to reject most of DIO electron tracks.
- Low-mass detector to reduce energy loss and multiple scattering, with excellent momentum resolution, < 200 keV/c.

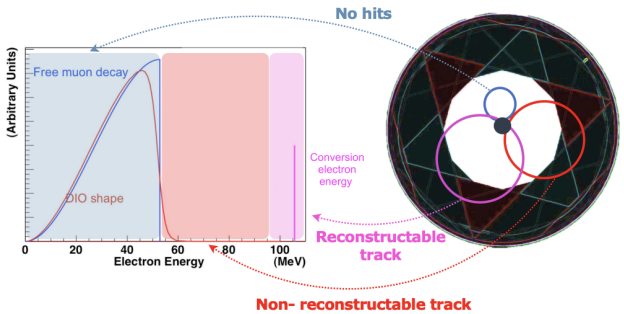

Straw tube Tracker

- Annular geometry to reject most of DIO electron tracks.
- Low-mass detector to reduce energy loss and multiple scattering, with excellent momentum resolution, < 200 keV/c.
- It consists of 18 stations. Each station is made by 2 planes, each plane by 6 panels, and each panel contains 96 straws.

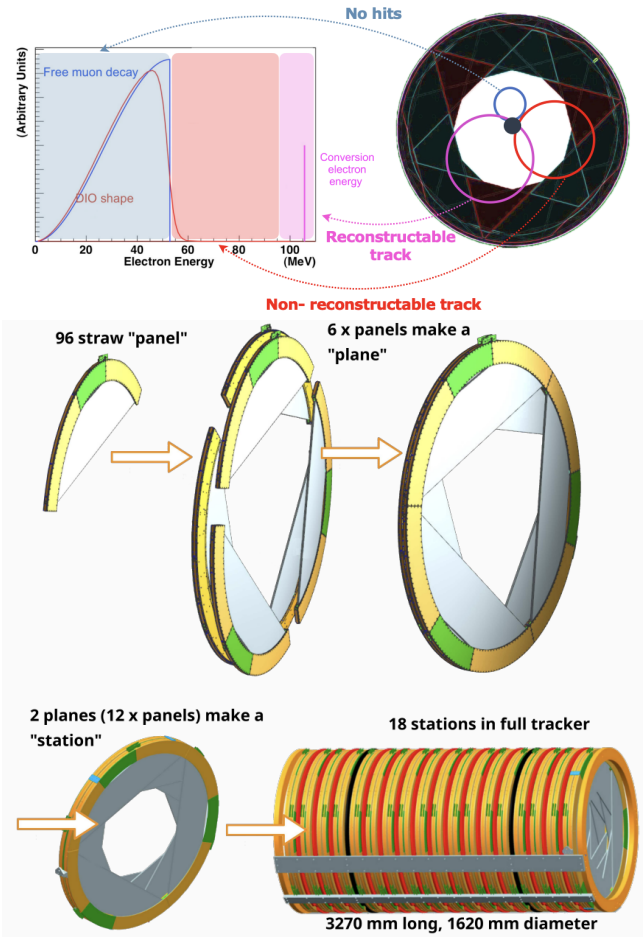

Straw tube Tracker

- Annular geometry to reject most of DIO electron tracks.
- Low-mass detector to reduce energy loss and multiple scattering, with excellent momentum resolution, < 200 keV/c.
- It consists of 18 stations. Each station is made by 2 planes, each plane by 6 panels, and each panel contains 96 straws.
- Each straw is made of 25 μm diameter gold plated tungsten sense wire centered in a 5 mm diameter aluminized mylar tubes. The straw length can vary from 40 to 120 cm.

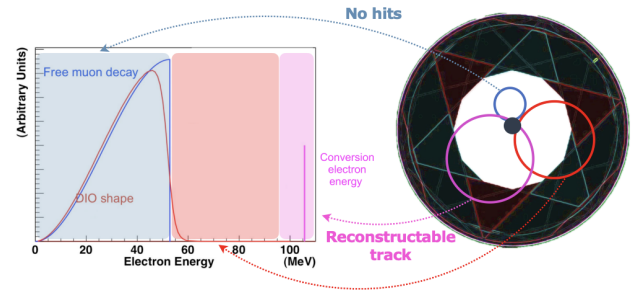

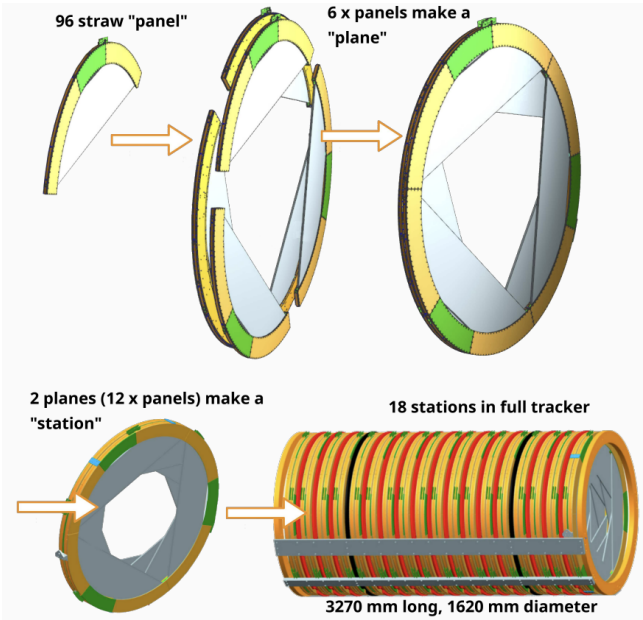

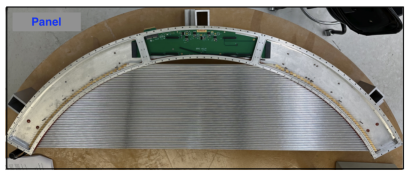

Straw tube Tracker

- Annular geometry to reject most of DIO electron tracks.
- Low-mass detector to reduce energy loss and multiple scattering, with excellent momentum resolution, < 200 keV/c.
- It consists of 18 stations. Each station is made by 2 planes, each plane by 6 panels, and each panel contains 96 straws.
- Each straw is made of 25 μm diameter gold plated tungsten sense wire centered in a 5 mm diameter aluminized mylar tubes. The straw length can vary from 40 to 120 cm.
- Each straw is filled with 80%:20% Ar:CO_2 gas.

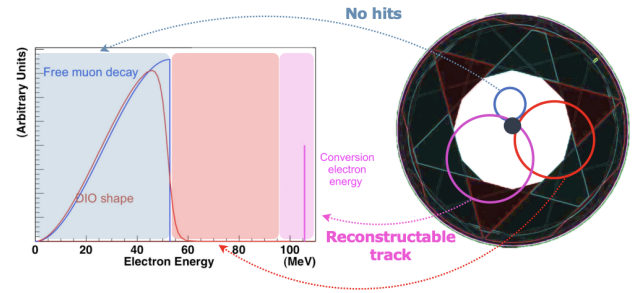

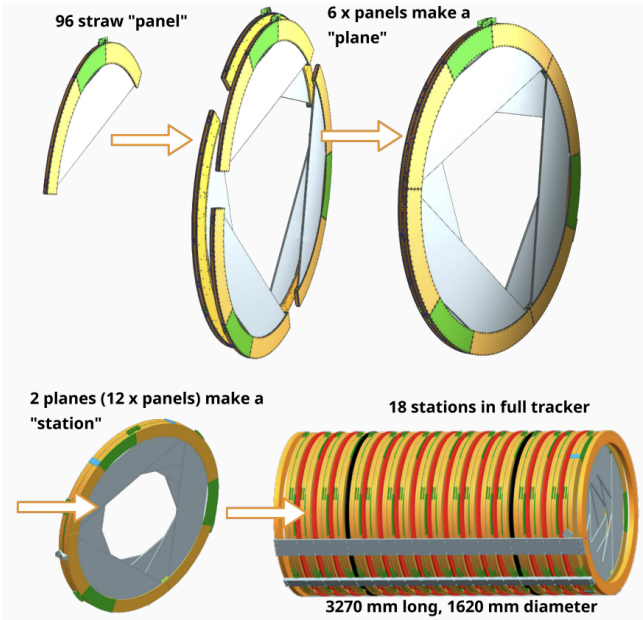

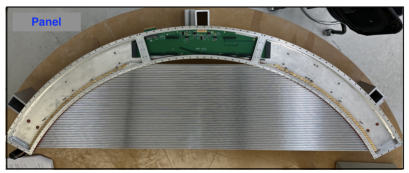

Electromagnetic Calorimeter

- Works in tandem with the tracker to confirm CE identification by providing powerful e/μ separation, and a fast seeding for track reconstruction.

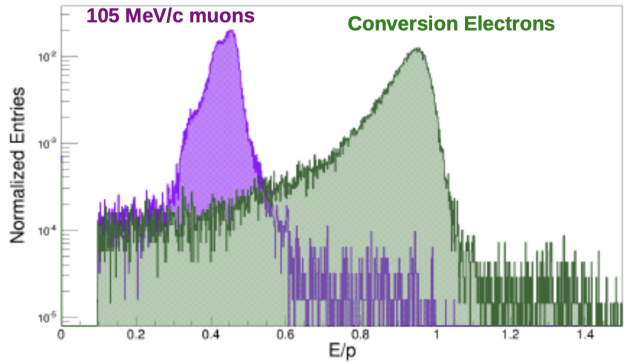

Electromagnetic Calorimeter

- Works in tandem with the tracker to confirm CE identification by providing powerful e/μ separation, and a fast seeding for track reconstruction.
- Consists of two annular disks with an internal radius of 35 cm and an external radius of 66 cm, separated by 70 cm.

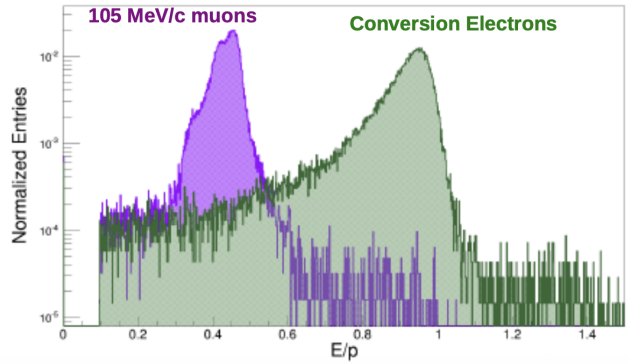

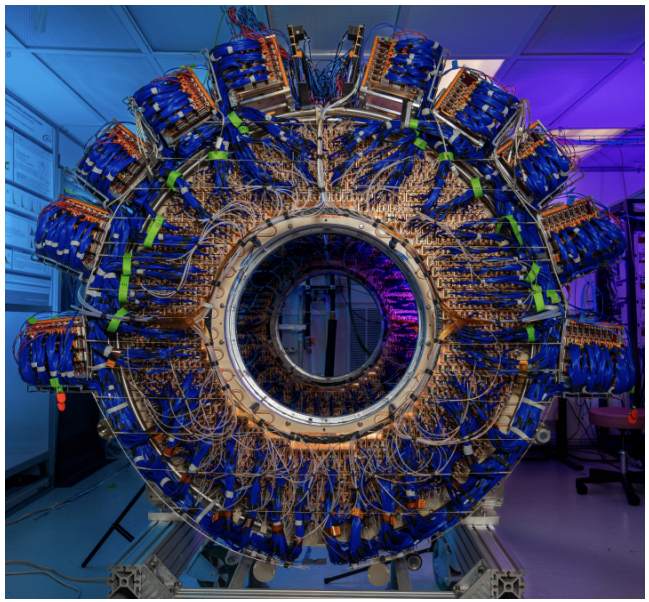

Electromagnetic Calorimeter

- Works in tandem with the tracker to confirm CE identification by providing powerful e/μ separation, and a fast seeding for track reconstruction.
- Consists of two annular disks with an internal radius of 35 cm and an external radius of 66 cm, separated by 70 cm.
- Each disk has 674 undoped CsI crystals, readout by SiPMs.

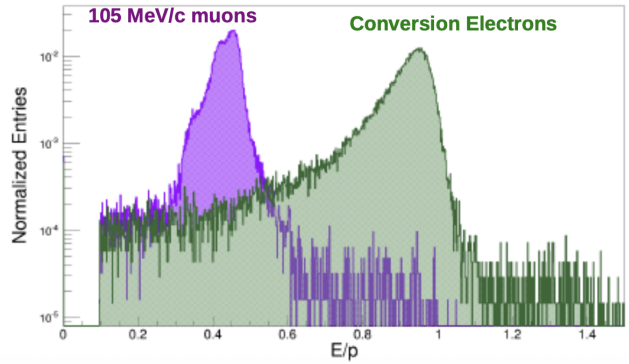

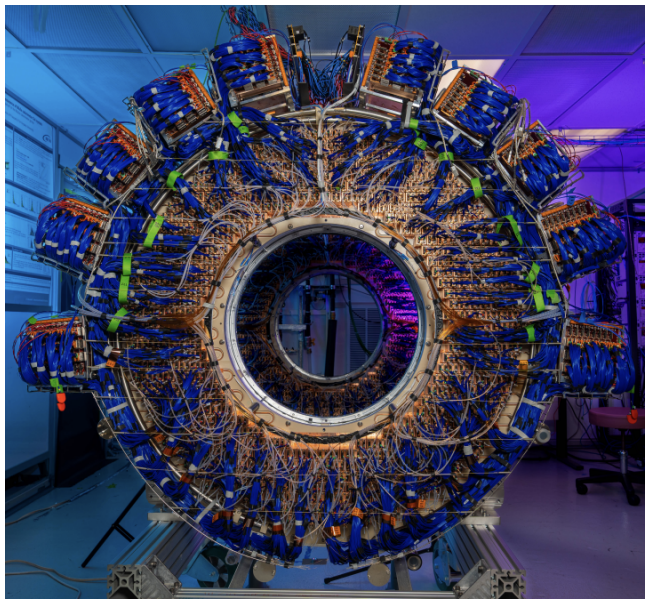

Electromagnetic Calorimeter

- Works in tandem with the tracker to confirm CE identification by providing powerful e/μ separation, and a fast seeding for track reconstruction.
- Consists of two annular disks with an internal radius of 35 cm and an external radius of 66 cm, separated by 70 cm.
- Each disk has 674 undoped CsI crystals, readout by SiPMs.
- Tests of the prototype using a 100 MeV e^- beam have demonstrated energy resolution $\Delta E/E = 16.4\%$ FWHM and time resolution $\sigma_t = 110$ ps [5].

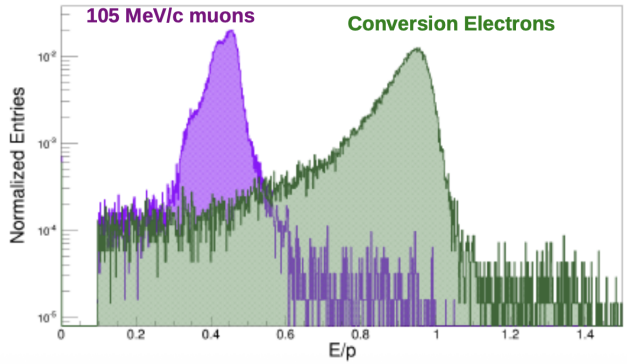

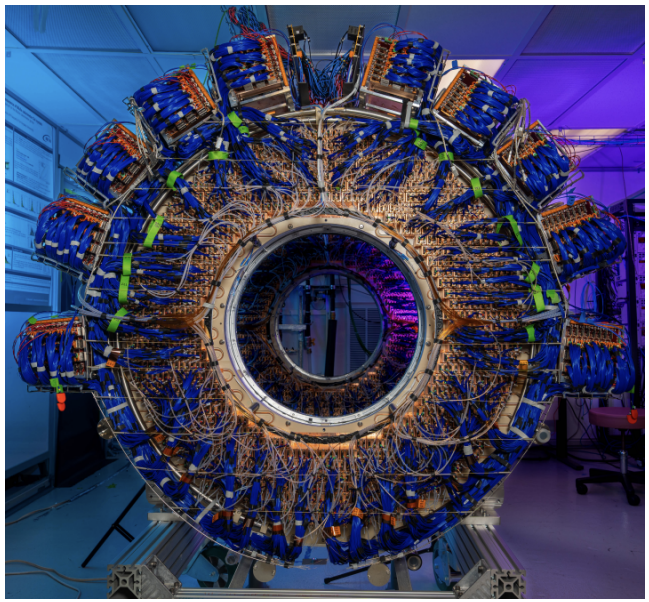

Cosmic Ray Veto System

- It covers the entire Detector Solenoid and part of the Transport Solenoid.

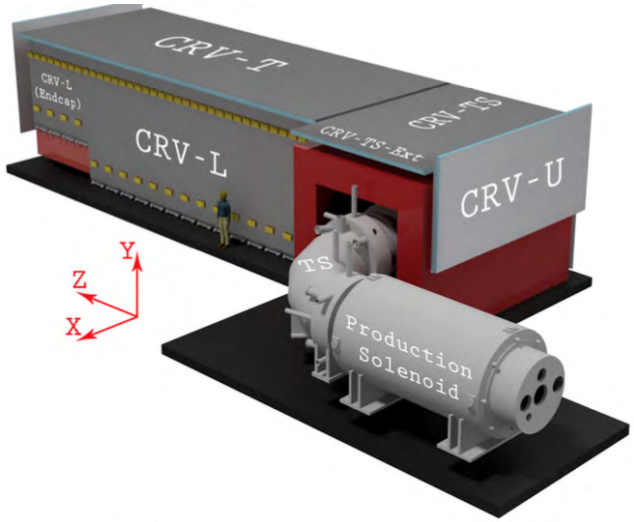

Cosmic Ray Veto System

- It covers the entire Detector Solenoid and part of the Transport Solenoid.
- Consists of multiple layers of long plastic scintillating counters, embedded with wavelength-shifting fibers and SiPMs at both ends for read-out.

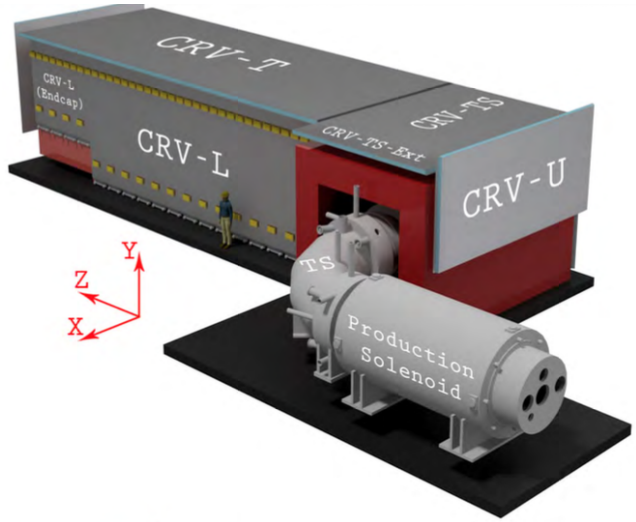

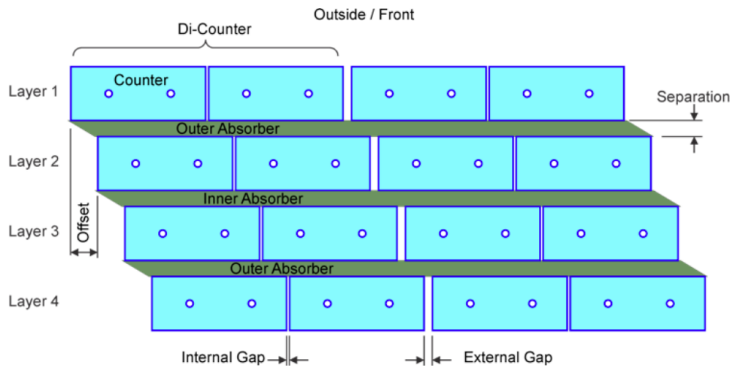

Cosmic Ray Veto System

- It covers the entire Detector Solenoid and part of the Transport Solenoid.
- Consists of multiple layers of long plastic scintillating counters, embedded with wavelength-shifting fibers and SiPMs at both ends for read-out.
- Counters are coated with TiO_2 to enhance internal reflections and improve light yield.

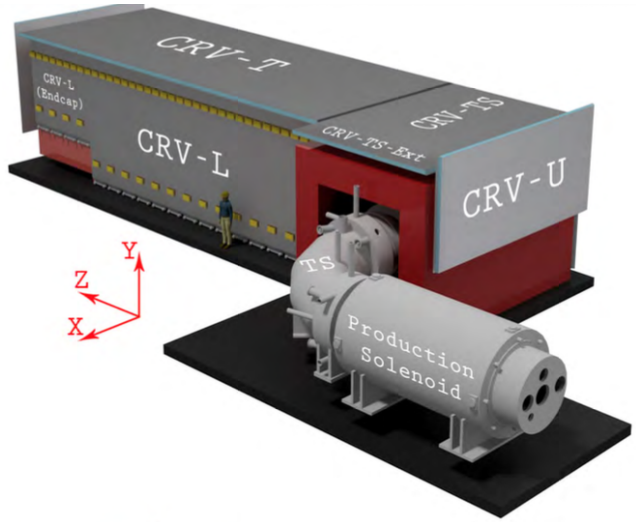

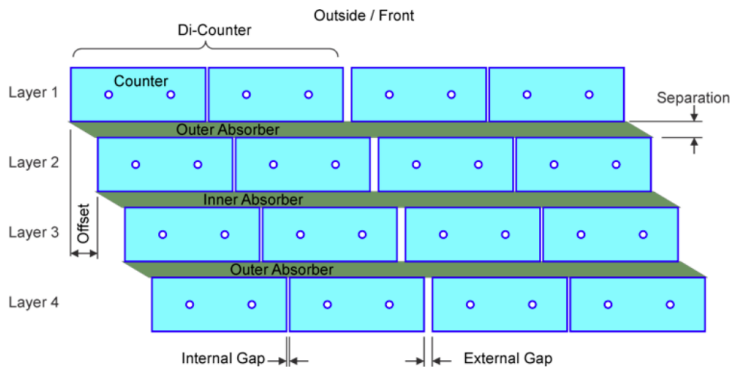

Cosmic Ray Veto System

- It covers the entire Detector Solenoid and part of the Transport Solenoid.
- Consists of multiple layers of long plastic scintillating counters, embedded with wavelength-shifting fibers and SiPMs at both ends for read-out.
- Counters are coated with TiO_2 to enhance internal reflections and improve light yield.
- When signals are detected simultaneously in adjacent counters across at least three of four layers, it is identified as a cosmic ray event.

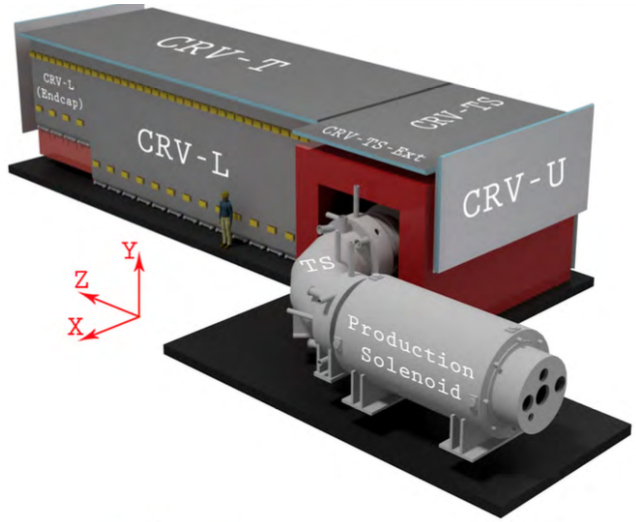

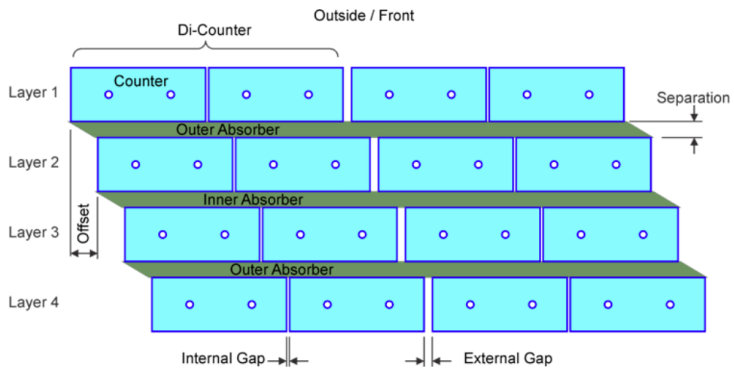

Cosmic Ray Veto System

- It covers the entire Detector Solenoid and part of the Transport Solenoid.
- Consists of multiple layers of long plastic scintillating counters, embedded with wavelength-shifting fibers and SiPMs at both ends for read-out.
- Counters are coated with TiO_2 to enhance internal reflections and improve light yield.
- When signals are detected simultaneously in adjacent counters across at least three of four layers, it is identified as a cosmic ray event.
- To achieve the desired experimental sensitivity, Mu2e CRV must be 99.99% efficient at rejecting cosmic rays.

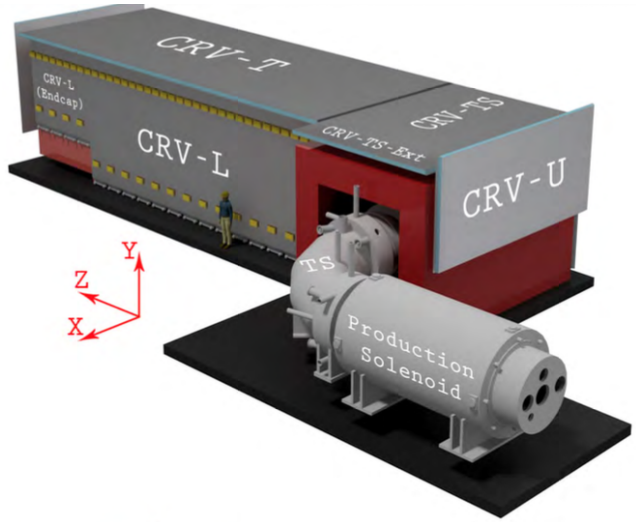

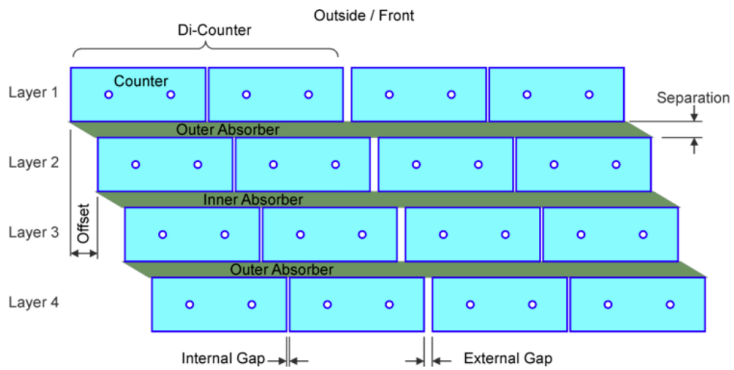

Stopping Target Monitor

- Positioned ∼35 m downstream of the stopping target, the STM provides the primary means of normalization for the experiment.

Stopping Target Monitor

- Positioned ∼35 m downstream of the stopping target, the STM provides the primary means of normalization for the experiment.
- Consists of a solid state HPGe and a scintillating $LaBr_3$ detector.

Stopping Target Monitor

- Positioned ∼35 m downstream of the stopping target, the STM provides the primary means of normalization for the experiment.
- Consists of a solid state HPGe and a scintillating $LaBr_3$ detector.
- It measures the rate of photons produced when negative muons interact with the ST.

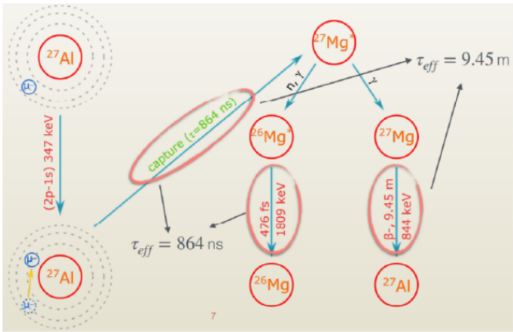

Stopping Target Monitor

- Positioned ∼35 m downstream of the stopping target, the STM provides the primary means of normalization for the experiment.
- Consists of a solid state HPGe and a scintillating $LaBr_3$ detector.
- It measures the rate of photons produced when negative muons interact with the ST.
- Here is an example spectrum from the AlCap experiment which measured photon spectra from muons stopping in aluminum, at low rates.

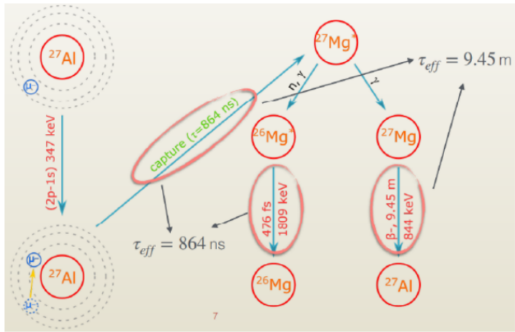

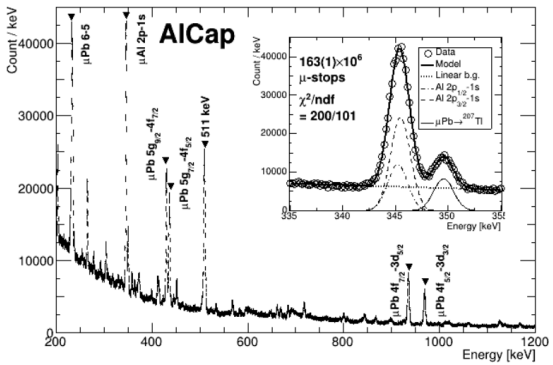

Status of the Experiment

Status: Solenoids

1. Production Solenoid: Fully assembled in winter 2024. Delivered to the Mu2e hall in August 2025.

Status: Solenoids

1. Production Solenoid: Fully assembled in winter 2024. Delivered to the Mu2e hall in August 2025.
2. Transport Solenoid: TSu was delivered in 12/23 and TSd in 2/24. Rotating collimator and antiproton absorber installed. Cryogenic system connection progressing.

Status: Solenoids

1. Production Solenoid: Fully assembled in winter 2024. Delivered to the Mu2e hall in August 2025.
2. Transport Solenoid: TSu was delivered in 12/23 and TSd in 2/24. Rotating collimator and antiproton absorber installed. Cryogenic system connection progressing.
3. Detector Solenoid: Inner bore inserted into cold mass and cold mass into vacuum vessel. Expected delivery end of 2025.

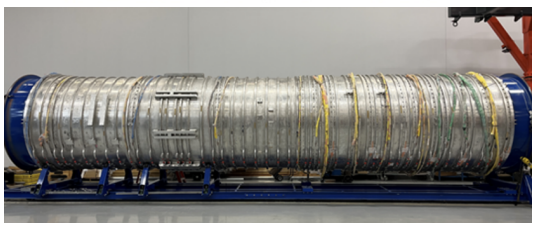

Status: Tracker

- Stations installation completed.

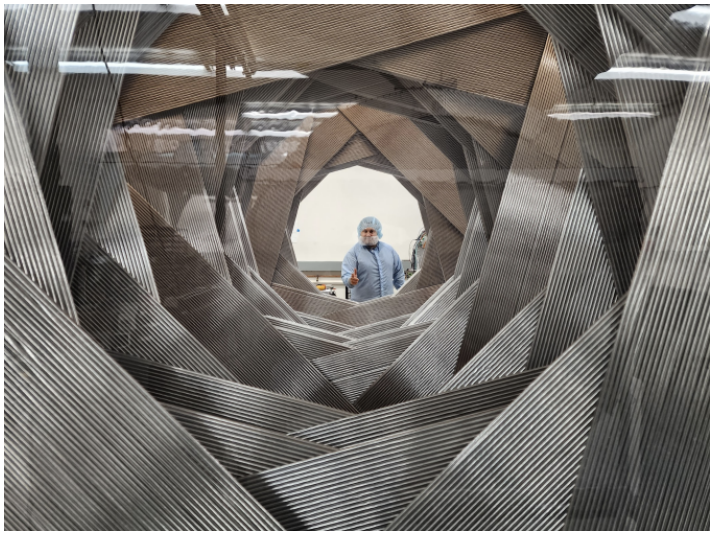

Status: Tracker

- Stations installation completed.
- Cosmic and noise runs currently being taken using the first assembled station.

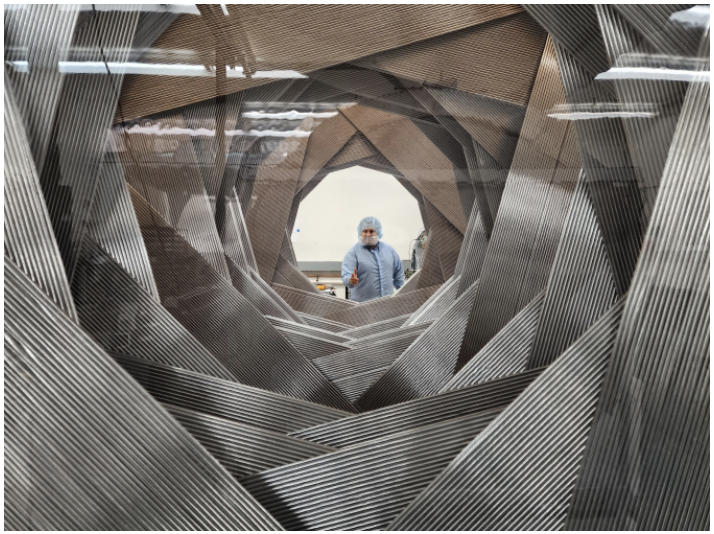

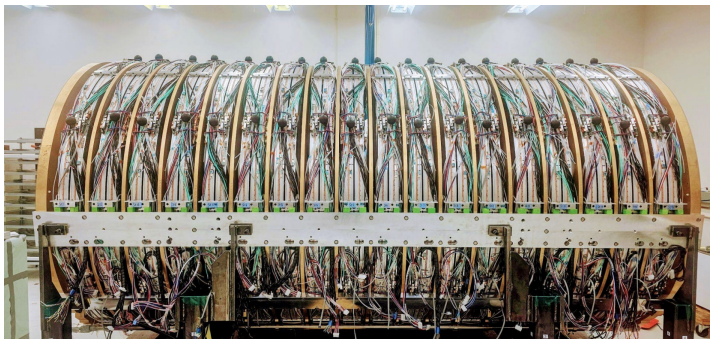

Status: Tracker

- Stations installation completed.
- Cosmic and noise runs currently being taken using the first assembled station.
- Tracker moved to the Mu2e hall and installed on the rails on 18/11/2025.

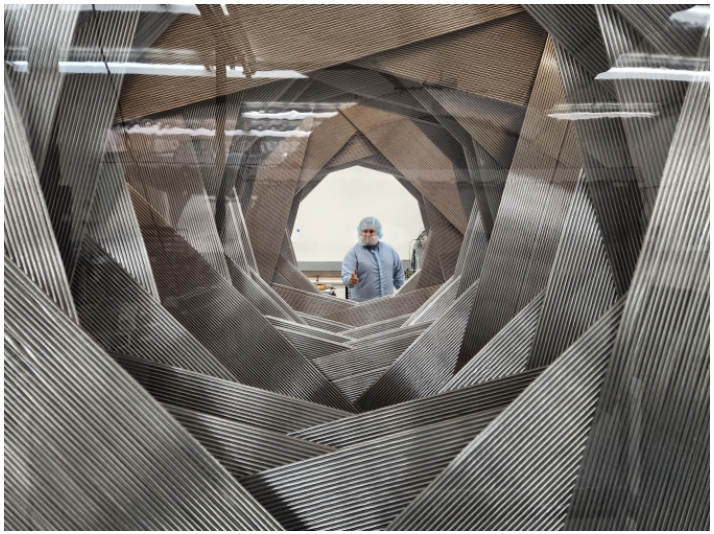

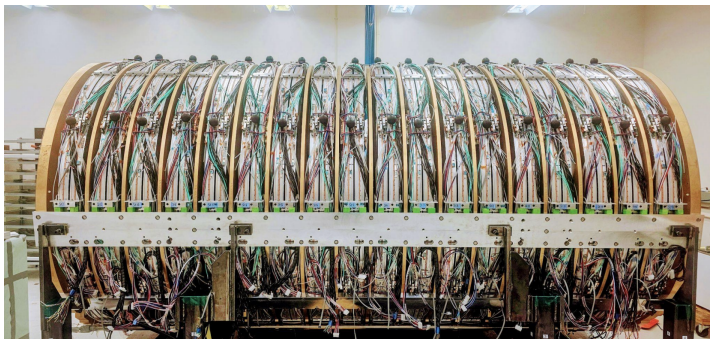

Status: Tracker moved to Mu2e Hall

Status: Tracker moved to Mu2e Hall

Status: Calorimeter

- The calorimeter disks were assembled, instrumented, and tested by June 2025.
- Fully calibrated. Successful readout of all channels and good data quality.
- Moved to the Mu2e Hall in Fall 2025.

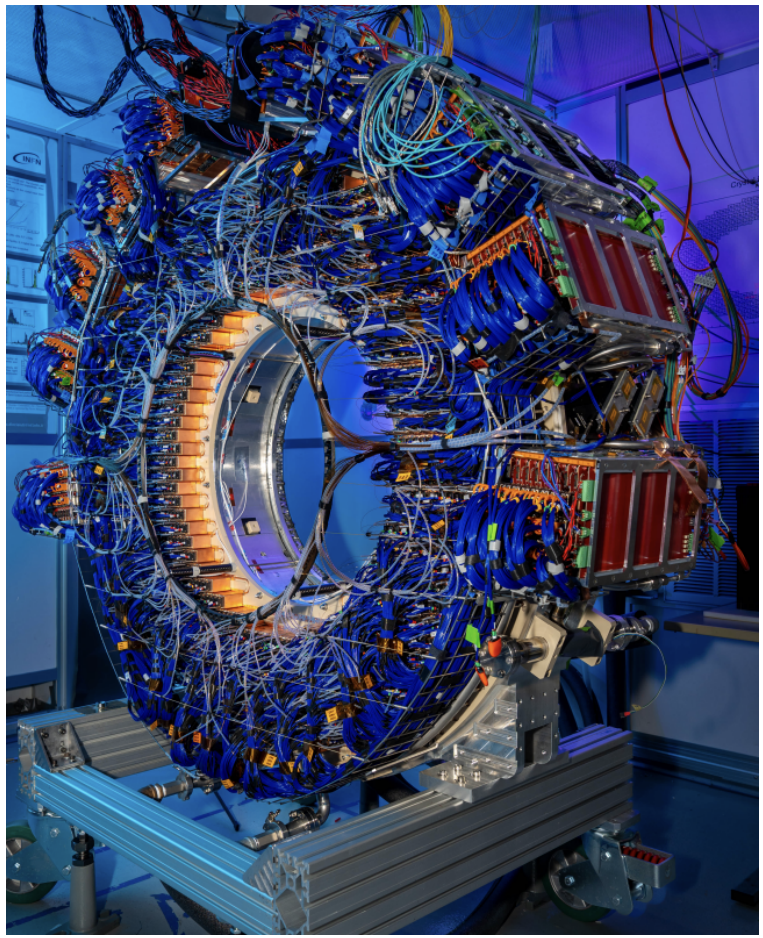

Calorimeter moved to the Mu2e Hall

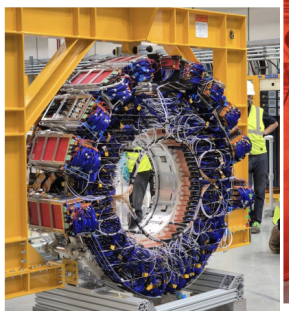

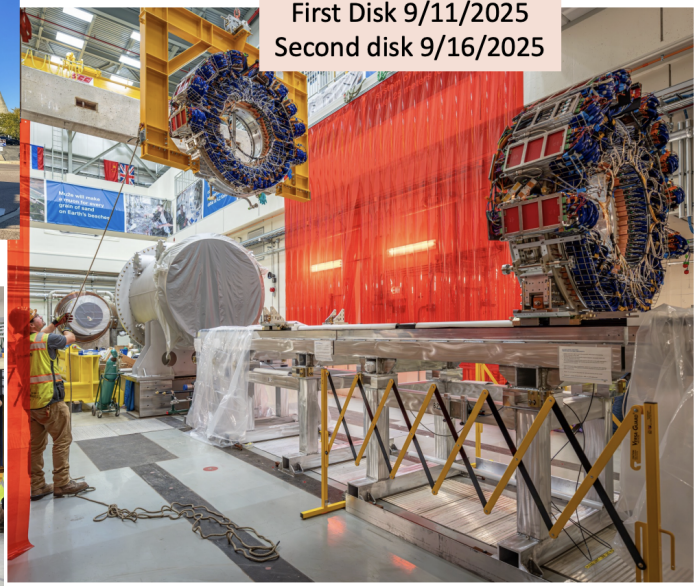

First Disk 9/11/2025
Second disk 9/16/2025

Status: CRV

- All the CRV modules have been constructed and are stored in Fermilab.
- All the counters (scintillator with fiber and SiPM) have been tested. VST is progressing well.
- Expected to be installed in the Mu2e hall in 2026.

Commissioning and Run Plan

- By end of 2025, we plan to start a commissioning cosmic run with the calorimeter and a fraction of the CRV.

Commissioning and Run Plan

- By end of 2025, we plan to start a commissioning cosmic run with the calorimeter and a fraction of the CRV.
- Installation of the tracker at the end of 2025, and start another cosmic run with the PS and TS in 2026.

Commissioning and Run Plan

- By end of 2025, we plan to start a commissioning cosmic run with the calorimeter and a fraction of the CRV.
- Installation of the tracker at the end of 2025, and start another cosmic run with the PS and TS in 2026.
- Perform in-situ calibration of both the main detectors.

Commissioning and Run Plan

- By end of 2025, we plan to start a commissioning cosmic run with the calorimeter and a fraction of the CRV.
- Installation of the tracker at the end of 2025, and start another cosmic run with the PS and TS in 2026.
- Perform in-situ calibration of both the main detectors.
- DS installation and commissioning, and another cosmic run in late 2026.

Commissioning and Run Plan

- By end of 2025, we plan to start a commissioning cosmic run with the calorimeter and a fraction of the CRV.
- Installation of the tracker at the end of 2025, and start another cosmic run with the PS and TS in 2026.
- Perform in-situ calibration of both the main detectors.
- DS installation and commissioning, and another cosmic run in late 2026.
- Physics Run I in 2027 for a few months before the Fermilab accelerator shutdown for PIP-II installation (January 2028).

Commissioning and Run Plan

- By end of 2025, we plan to start a commissioning cosmic run with the calorimeter and a fraction of the CRV.
- Installation of the tracker at the end of 2025, and start another cosmic run with the PS and TS in 2026.
- Perform in-situ calibration of both the main detectors.
- DS installation and commissioning, and another cosmic run in late 2026.
- Physics Run I in 2027 for a few months before the Fermilab accelerator shutdown for PIP-II installation (January 2028).
- Aim to collect upto 10% of the total protons on target. The sensitivity goals are:
  - At 90% C.L, $R_{\mu e} < 6 \times 10^{-16}$
  - 5σ discovery limit, $R_{\mu e} < 1.2 \times 10^{-15}$ with a total expected background of $\sim$0.1 events.

Commissioning and Run Plan

- By end of 2025, we plan to start a commissioning cosmic run with the calorimeter and a fraction of the CRV.
- Installation of the tracker at the end of 2025, and start another cosmic run with the PS and TS in 2026.
- Perform in-situ calibration of both the main detectors.
- DS installation and commissioning, and another cosmic run in late 2026.
- Physics Run I in 2027 for a few months before the Fermilab accelerator shutdown for PIP-II installation (January 2028).
- Aim to collect upto 10% of the total protons on target. The sensitivity goals are:
  - At 90% C.L, $R_{\mu e} < 6 \times 10^{-16}$
  - 5σ discovery limit, $R_{\mu e} < 1.2 \times 10^{-15}$ with a total expected background of $\sim$0.1 events.
- Delay in the delivery of the DS could impact run time and sensitivity. Contingency plans with reduced CRV coverage are currently being explored.

Summary

- Mu2e aims to improve up to four orders of magnitude the current limits of the CLFV search with muon-to-electron conversion in a nuclear field.

Summary

- Mu2e aims to improve up to four orders of magnitude the current limits of the CLFV search with muon-to-electron conversion in a nuclear field.
- Detection of a CLFV process will be an indisputable evidence of New Physics.

Summary

- Mu2e aims to improve up to four orders of magnitude the current limits of the CLFV search with muon-to-electron conversion in a nuclear field.
- Detection of a CLFV process will be an indisputable evidence of New Physics.
- One year commissioning run is expected to start in late 2025 followed by physics run in 2027 before the 2-year long accelerator shutdown.

Summary

- Mu2e aims to improve up to four orders of magnitude the current limits of the CLFV search with muon-to-electron conversion in a nuclear field.
- Detection of a CLFV process will be an indisputable evidence of New Physics.
- One year commissioning run is expected to start in late 2025 followed by physics run in 2027 before the 2-year long accelerator shutdown.
- Run I goal is to collect at least 10% of the total protons on target. Simulations show that it will improve the current sensitivity by $\mathcal{O}(10^3)$.

Mu2e Collaboration

Back-up Slides

CLFV model-independent Lagrangian

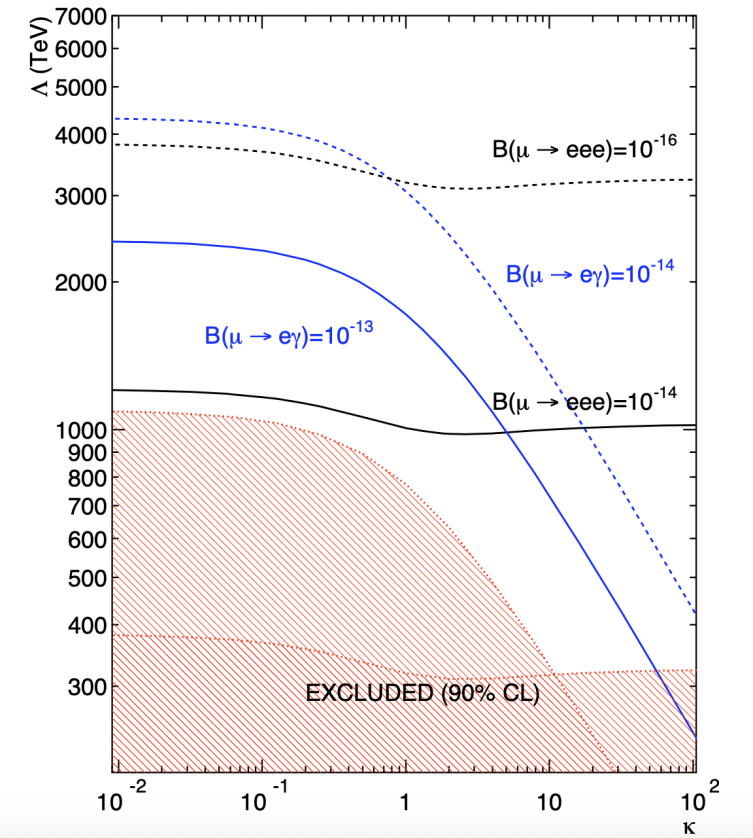

If the new physics is best captured by the following "leptons-only" effective Lagrangian:

$$\mathcal{L}_{CLFV} = \frac{m_\mu}{(1+\kappa)\Lambda^2}\bar{\mu}_R\sigma_{\mu\nu}e_L F^{\mu\nu} + \frac{\kappa}{(1+\kappa)\Lambda^2}\bar{\mu}_L\gamma_\mu e_L(\bar{e}\gamma^\mu e) + h.c$$

CLFV model-independent Lagrangian

An alternative EFT formulation, proposed by Adrian Signer et al,

$$\mathcal{L}_{SMEFT} = \mathcal{L}_{SM} + \frac{1}{\Lambda} C^{(5)} Q^{(5)} + \frac{1}{\Lambda^2} C_i^{(6)} Q_i^{(6)} + ...$$

where the Wilson coefficients at the high scale, $C_i^{(6)}(\mu)$ depend on the energy scale μ. CLFV processes take place at an even lower scale than M_{EW}, $(m_\mu, m_\tau \ll M_{EW} \ll \Lambda)$. Thus they are better described by LEFT:

$$\mathcal{L}_{LEFT} = \mathcal{L}_{QED} + \mathcal{L}_{QCD} + \frac{1}{M_{EW}} \sum_j \mathscr{C}_j^{(5)} \mathscr{L}_j^{(5)} + \frac{1}{M_{EW}^2} \mathscr{C}_j^{(6)} \mathscr{L}_j^{(6)} + ...$$

$\mathscr{C}(_\mu, _\tau)$ at low energies can be determined from the SMEFT coefficients $\mathcal{C}(M_{EW})$ via matching, followed by RGE evolution down to $\mu \sim m_\mu$. Mixing can transfer strength from the dipole operators to the four fermion operators. Large $\log(\Lambda/\mu)$ factors can enhance loop-induced contributions, making certain contact interaction terms numerically significant at low energies.

CLFV model-independent Lagrangian

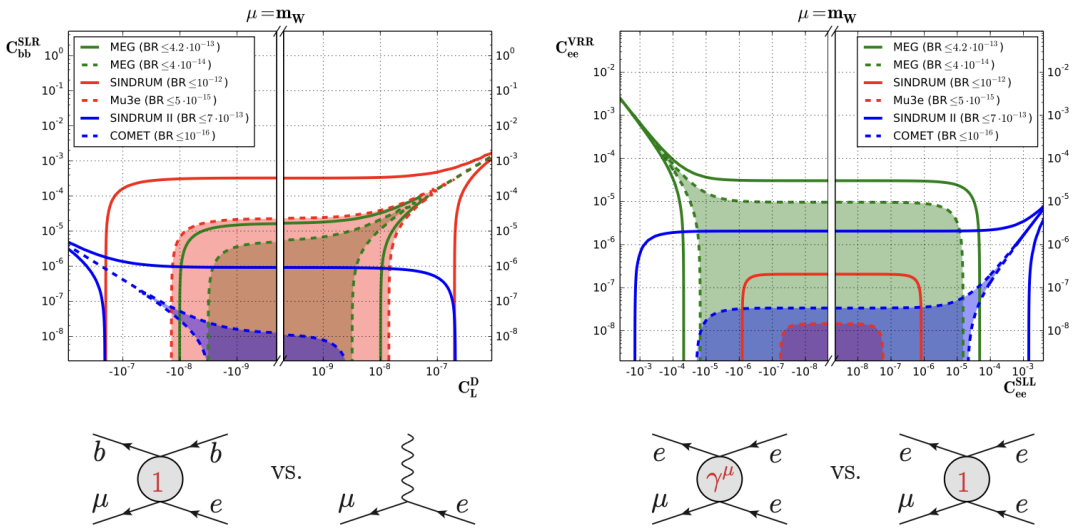

Figure 2: Comparison of limits obtained from the muon CLFV channels on Wilson coefficients $\mathscr{C}(M_{EW})$ of LEFT. Left panel: scalar four-fermion operator involving b quarks, C_{bb}^{SLR} v/s dipole operator, C_L^D; right panel: vector four-fermion operator C_{ee}^{VRR} v/s scalar four-fermion operator $C_e^{SLL}e$. The expected improvement in constraining the limits on the operators due to future measurements are indicated by the dashed lines [6].

Physics reach of $\mu N \to eN$

	AC	RVV2	AKM	δLL	FBMSSM	LHT	RS
$D^0 - \bar{D}^0$	★★★	★	★	★	★	★★★	?
ϵ_K	★	★★★	★★★	★	★	★★	★★★
$S_{\psi\phi}$	★★★	★★★	★★★	★	★	★★★	★★★
$S_{\phi K_S}$	★★★	★★	★	★★★	★★★	★	?
$A_{\rm CP}\,(B \to X_s\gamma)$	★	★	★	★★★	★★★	★	?
$A_{7,8}(B \to K^*\mu^+\mu^-)$	★	★	★	★★★	★★★	★★	?
$A_9(B \to K^*\mu^+\mu^-)$	★	★	★	★	★	★	?
$B \to K^{(*)}\nu\bar{\nu}$	★	★	★	★	★	★	★
$B_s \to \mu^+\mu^-$	★★★	★★★	★★★	★★★	★★★	★	★
$K^+ \to \pi^+\nu\bar{\nu}$	★	★	★	★	★	★★★	★★★
$K_L \to \pi^0\nu\bar{\nu}$	★	★	★	★	★	★★★	★★★
$\mu \to e\gamma$	★★★	★★★	★★★	★★★	★★★	★★★	★★★
$\tau \to \mu\gamma$	★★★	★★★	★	★★★	★★★	★★★	★★★
$\mu + N \to e + N$	★★★	★★★	★★★	★★★	★★★	★★★	★★★
d_n	★★★	★★★	★★★	★★	★★★	★	★★★
d_e	★★★	★★★	★★	★	★★★	★	★★★
$(g-2)_\mu$	★★★	★★★	★★	★★★	★★★	★	?

Figure 3: "DNA" of flavour physics effects for the most interesting observables in a selection of SUSY and non-SUSY models FFF signals large effects, 3 red stars: two blue stars: visible but small effects and 1 black star implies that the given model does not predict sizable effects in that observable [7].

CLFV with τ leptons

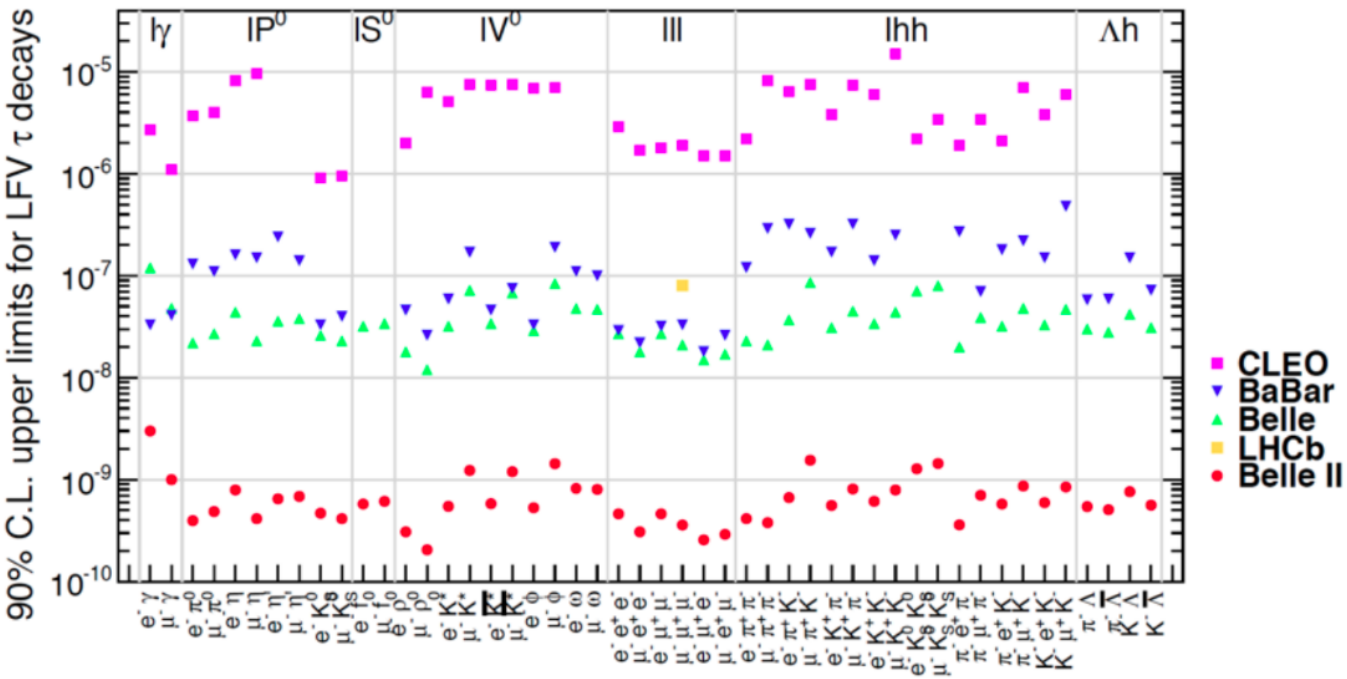

Fermilab Accelerator Overview

- Linac: Protons are generated and accelerated to a few hundred MeV.
- Booster: Accelerates protons up to 8 GeV.
- Recycler Ring: Re-bunches the protons into narrow bunches as per Mu2e requirements.
- Delivery Ring: Proton bunches prepared for resonant slow extraction.
- Proton beam is delivered to Mu2e for about 0.4 s every 1.4 s Main Injector cycle.
- They arrive at the production target in microbunches spaced about 1.7 μs apart. Each microbunch is 250 ns wide.

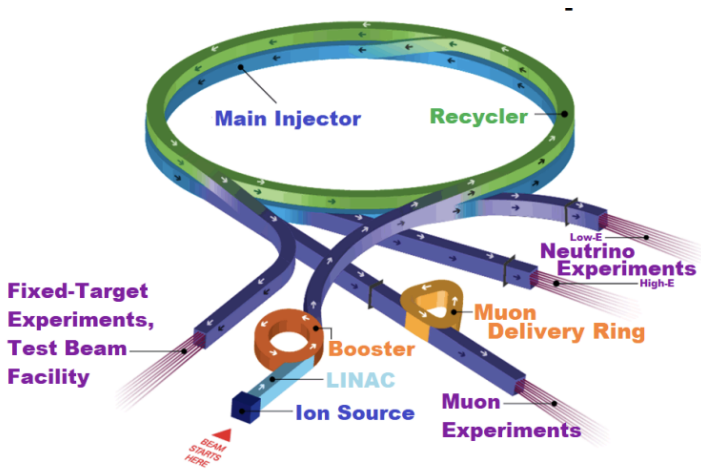

Mu2e beamline

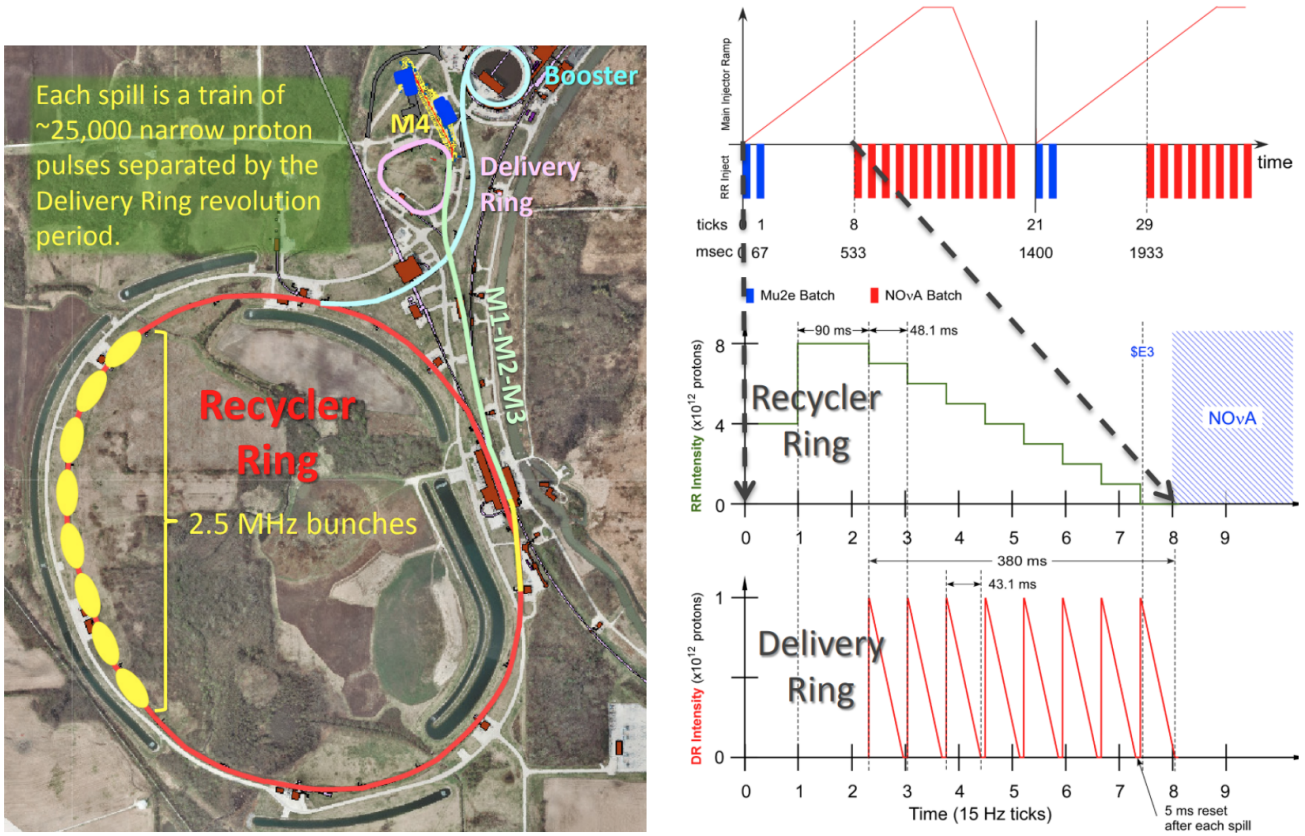

Figure 4: Fermilab accelerator overview. Figure (a) shows a labeled map of the Fermilab accelerator facilities with the Booster, Recycler, and Delivery rings shown. The M4 beamline connects the Delivery ring to the Mu2e building. Figure (b) gives an overview of the timing of proton pulses as they move through the Fermilab accelerator system. The three plots show the timing structure of how proton pulses are extracted from the Booster ring, rebunched in the Recycler ring, and then transferred to the Delivery ring, respectively.

Mu2e Run I plan

Running Mode	Mean Proton Pulse Intensity	Running Time (s)	N (POT)	N (Stopped Muons)
Low intensity	1.6×10^7	9.5×10^6	2.9×10^{19}	4.6×10^{16}
High intensity	3.9×10^7	1.6×10^6	9.0×10^{18}	1.4×10^{16}
Total		11.1×10^6	3.8×10^{19}	6.0×10^{16}

Figure 5: Expected running time, proton counts, and stopped muon counts for Mu2e Run I. The running time is the time, in seconds, during which the experiment is running and taking data. The numbers in the last two columns do not include the trigger, reconstruction, and selection efficiency [4].

Mu2e background estimate for Run I

Channel	Mu2e Run I
SES	2.4×10^{-16}
Cosmic rays	0.046 ± 0.010 (stat) ± 0.009 (syst)
DIO	0.038 ± 0.002 (stat) $^{+0.025}_{-0.015}$ (syst)
Antiprotons	0.010 ± 0.003 (stat) ± 0.010 (syst)
RPC in-time	0.010 ± 0.002 (stat) $^{+0.001}_{-0.003}$ (syst)
RPC out-of-time ($\zeta = 10^{-10}$)	$\left(1.2 \pm 0.1 \text{ (stat) } ^{+0.1}_{-0.3} \text{ (syst)}\right) \times 10^{-3}$
RMC	$< 2.4 \times 10^{-3}$
Decays in flight	$< 2 \times 10^{-3}$
Beam electrons	$< 1 \times 10^{-3}$
Total	0.105 ± 0.032

Figure 6: Background summary and SES using the optimized signal momentum and time window, $103.60 < p < 104.90$ MeV/c and $640 < T_0 < 1650$ ns [4].

Why Al stopping target

Practical Advantages	Physics Advantages
Chemically Stable	Conversion energy such that only tiny fraction of photons produced by muon radiative capture.
Available in required size/shape/thickness	Muon lifetime long compared to transit time of prompt backgrounds.
Low cost	Conversion rate increases with atomic number, reaching maximum at Se and Sb, then drops. Lifetime of muonic atoms decreases with increasing atomic number.
	Lifetime of muonic atom sits in "goldilocks" region i.e. neither longer than 1700 ns pulse spacing and greater than our pionic live gate.

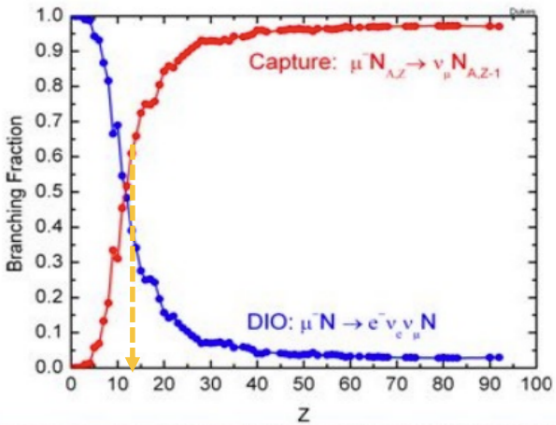

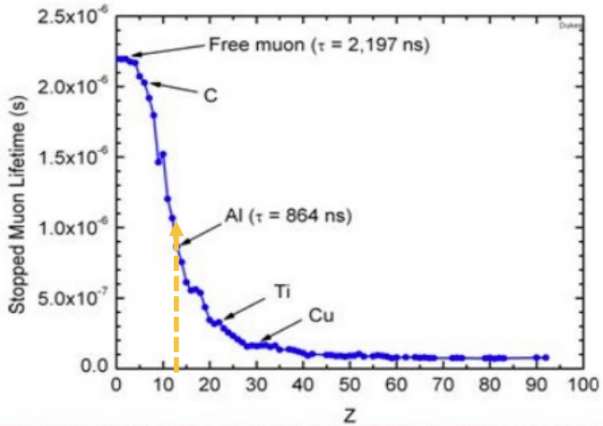

The lifetime of a muon in a muonic atom decreases with increasing atomic number.

Straw tube tracker

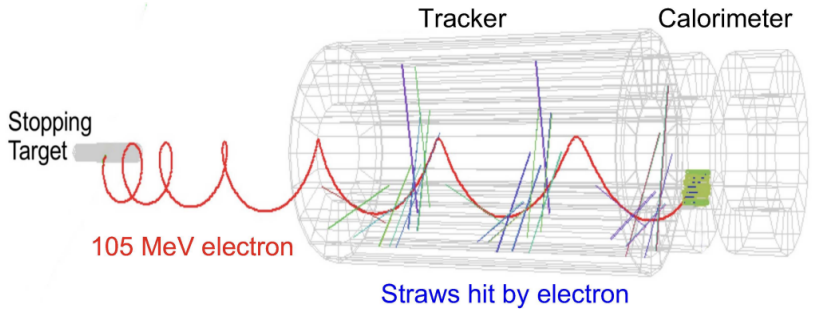

- 105 MeV signal makes 1.5-3 turns
  - ∼40 straws hit on average
- High pileup rate (∼100 KHz/straw)
  - >5 GHz of stopped muons
  - No hardware trigger
- No external or event t_0 constraint
  - muons are pulsed, but decay time is random

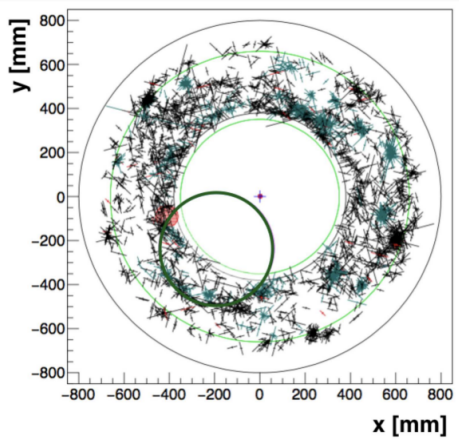

Simulated straw hits in one ∼1 μs event with CE (green line)

Mu2e simulation*

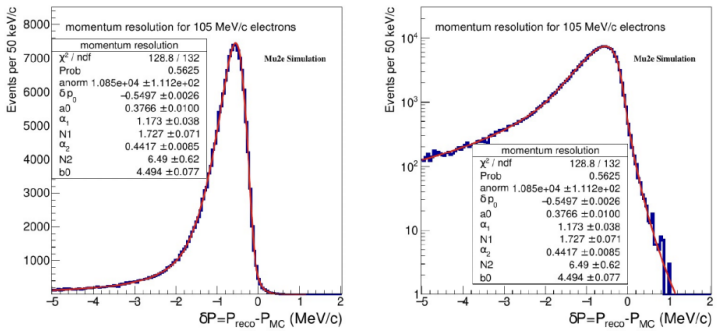

Straw tube tracker

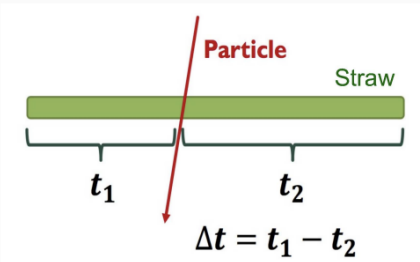

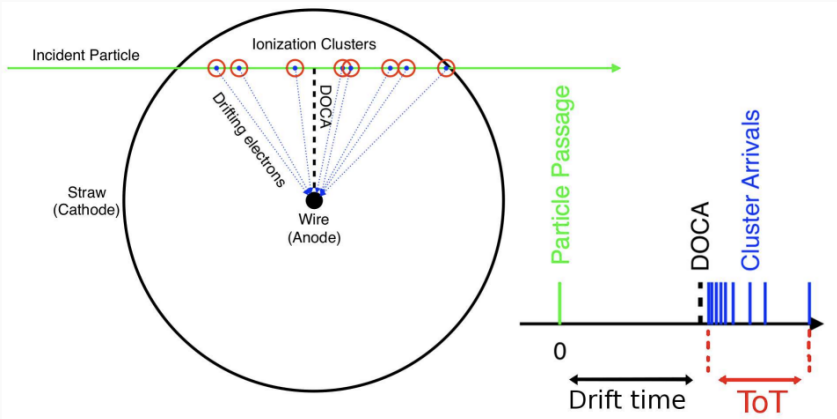

- Drift time → radial resolution ∼250 μm
- Time division → longitudinal resolution ∼4 cm
- Time-over-threshold → Measure of path length / radius independent of t_0
- Digitize waveform to reject highly ionizing backgrounds

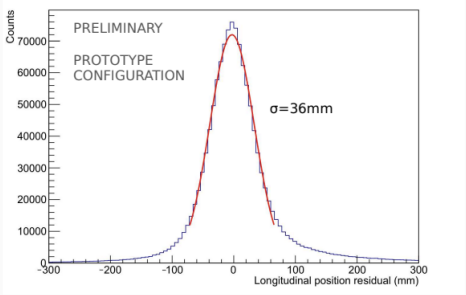

Longitudinal resolution, middle 80% of straw length (VST data), requirement <40 mm

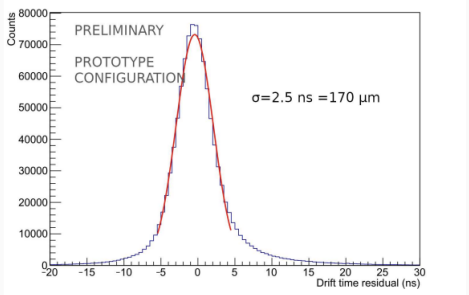

Drift resolution, excluding inner 0.5mm (VST data), requirement <250 mm

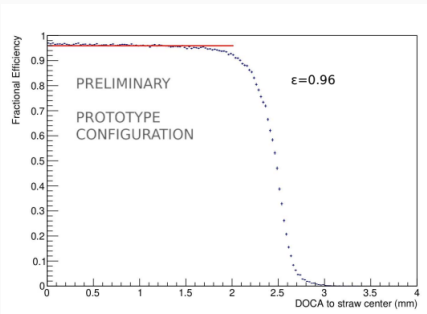

Efficiency vs distance to wire (VST data), requirement >90%

Tracker VST

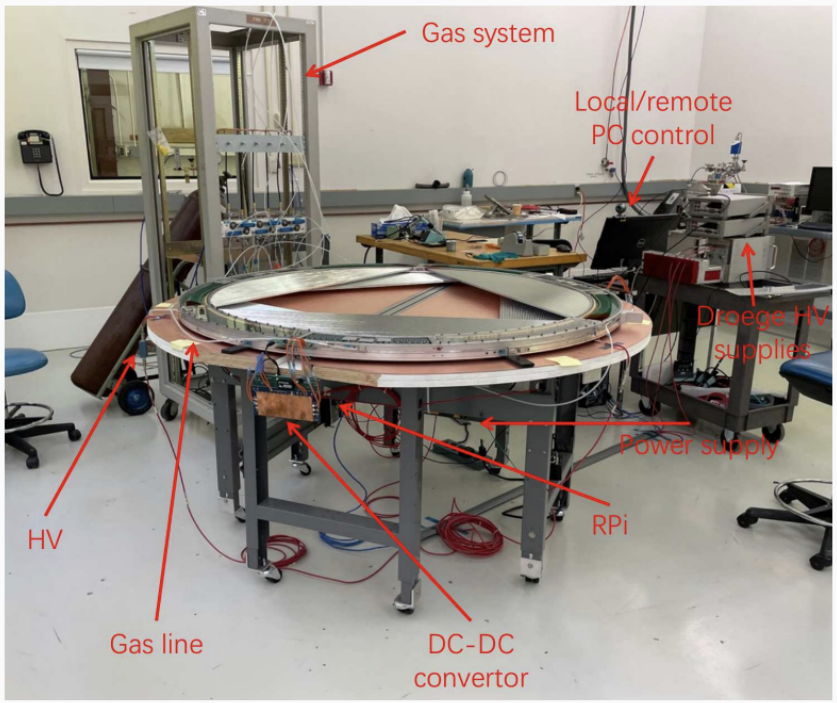

- 'vertical slice': Testing full chain from straws to readout to processed data on disk
- Six fully instrumented pre-production panels (576 straws) in plane configuration with associated HV/gas/cooling infrastructure
- Read out by streaming DAQ over optical fiber
- Source and cosmic ray data taken in several configurations
- Demonstrates performance under realistic conditions

Calorimeter design

- 674 CsI crystals/disk
- 1348 SiPM units/disk
- 1348 FEE units/disk
- 674 ROU units/disk
- 338 FEE-MZB Cables/disk
- 70 MZB boards/disk
- 70 DIRAC boards/disk
- 1 Source system
- 1 Laser system
- 8 x 110 Laser Fibers/disk

- Large mechanical parts
  - → Al Support disks
  - → FEE PEEK plate
  - → Carbon Fiber ring/pla
  - → source/cooling lines
  - → Feet and crates

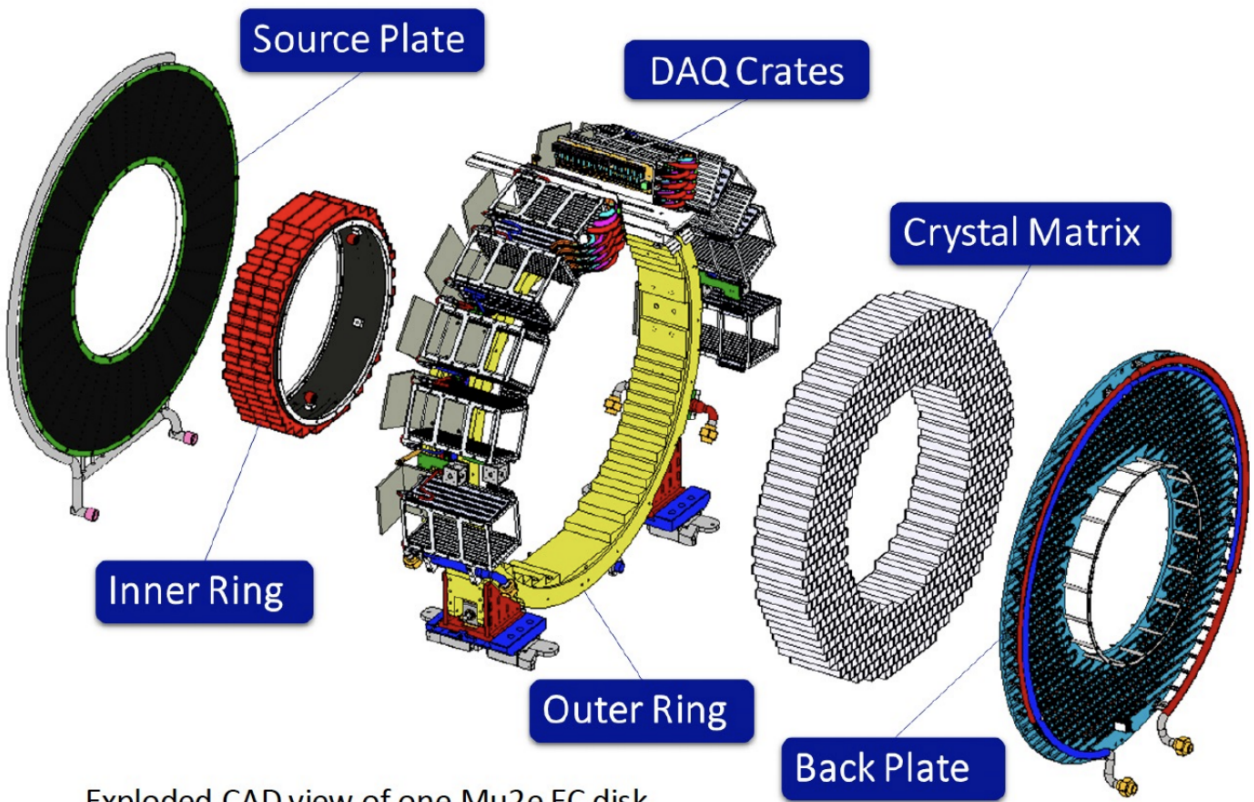

Exploded CAD view of one Mu2e EC disk

Module 0

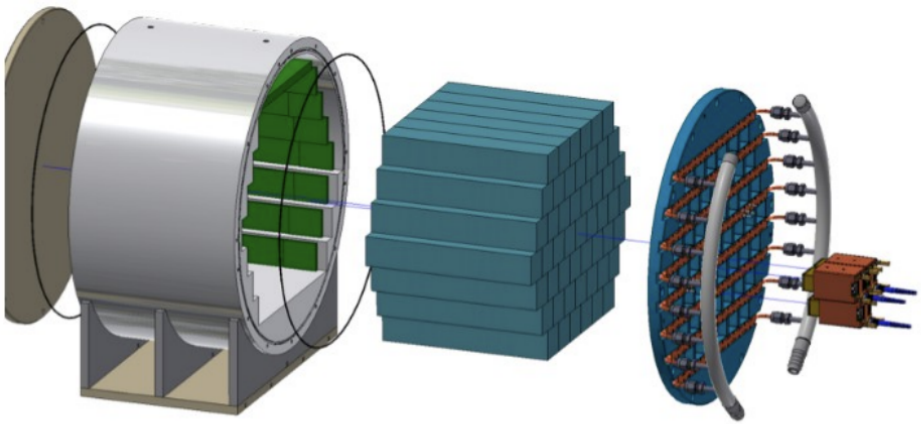

A **module 0** prototype with

- 51 crystals
- 102 SiPMs+FEE boards
- a commercial digitizer
- Cooling lines for SiPMs

The 2017 test with a beam in Frascati has measured for 100 MeV e- with 50° impact angle*:

σ_E/E = 7.3%

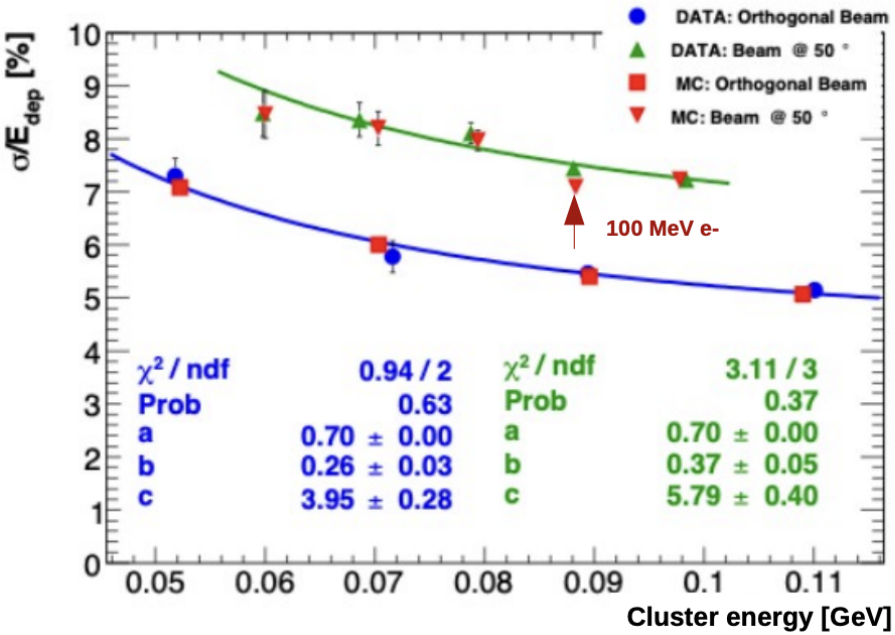

σ_t/t = 230 ps (only 1 sensor)

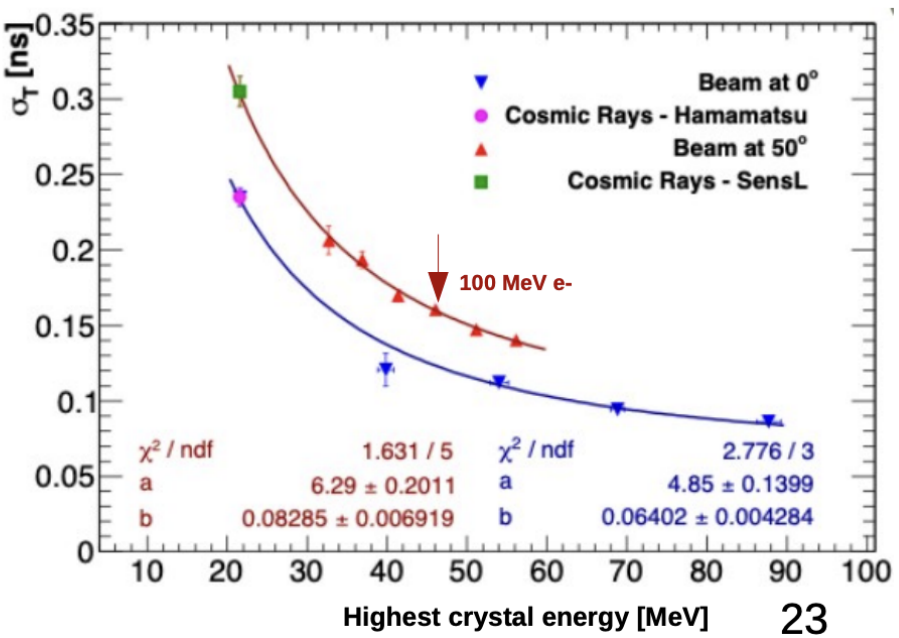

23

ECAL calibration

Radioactive liquid pipes

Laser system

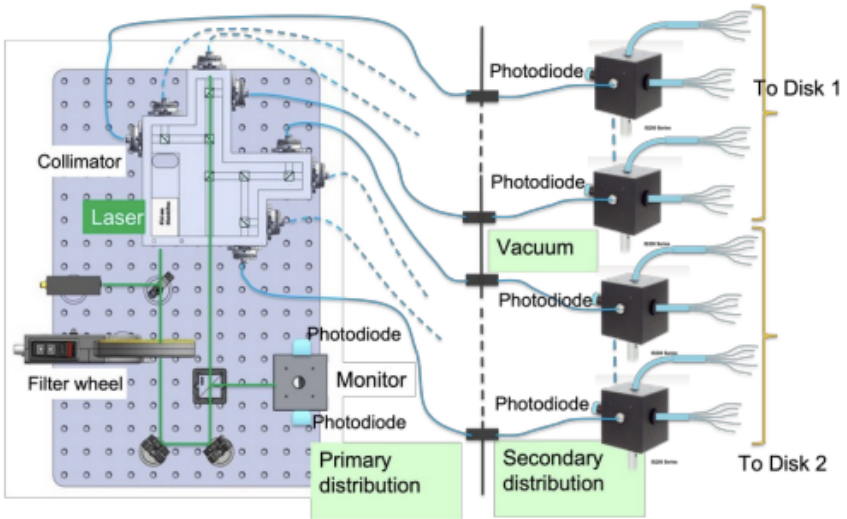

COSMIC RAY VETO (CRV)

- Vetoes cosmic ray muons that produce conversion-like backgrounds (~once/day)
- Covers entire Detector Solenoid (DS) and half of the Transport Solenoid (TS)
- 4 overlapping layers of extruded polystyrene scintillator bars, separated by ~ 10 mm absorber
  - 2 wavelength shifting (WLS) fibers per bar
  - Silicon photomultiplier (SiPM) readout, most modules on both ends
  - 125 ns veto when 3/4 layers hit (localized in space and time)
- High efficiency (>99.99%) veto, help to reduce total background over the entire experiment to <0.5 event (about half is cosmic background, still the main background of Mu2e)

Simulated cosmic event that produces 105 MeV electron when interacting with the stopping target.

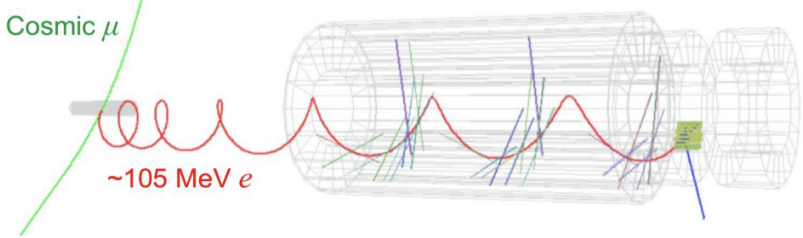

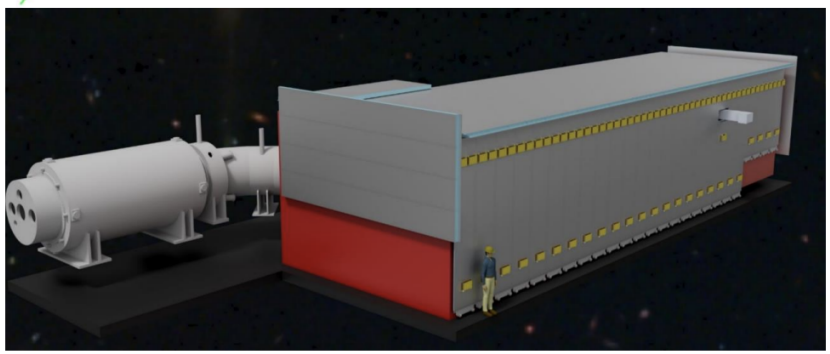

overview of the CRV

Extruded plastic scintillator bar

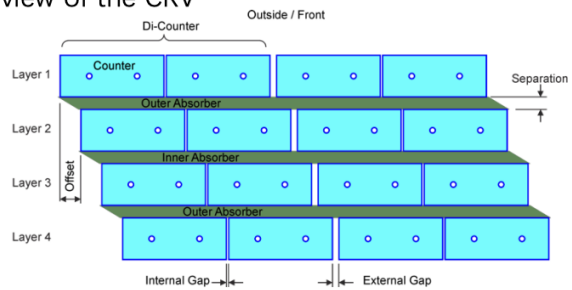

Mu2e event reconstruction

- From MC, $> 90\%$ of the hits in an event are from low energy e^+/e^- and protons. They have to be flagged as background (FBH) prior to the track reconstruction.
- We cluster the hits within a time window to form *TimeClusters* assuming that such hits are made by the same particle.
- Hits from the *TimeClusters* are used to form *helices*.
- Final parameters of the *track* are determined by the Kalman fit.

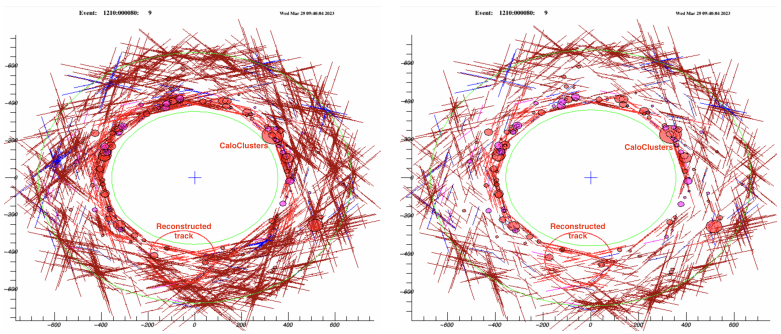

(a) Before FBH (b) After FBH

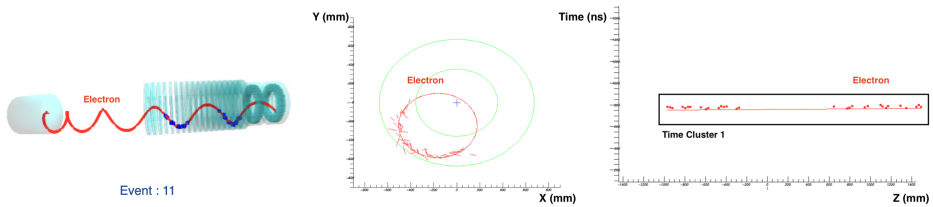

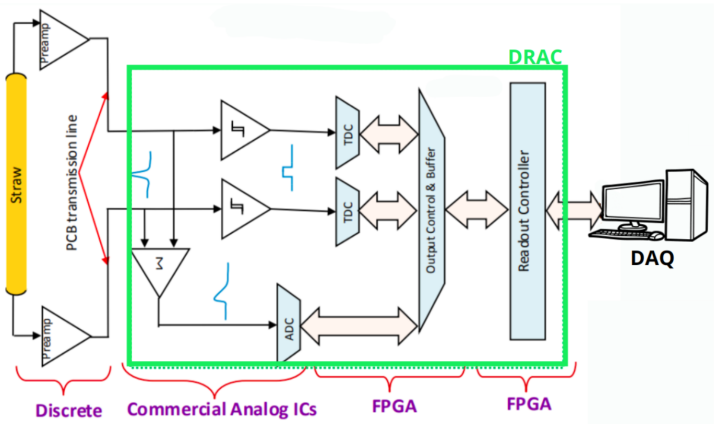

Figure 8: Signal flow in tracker straw

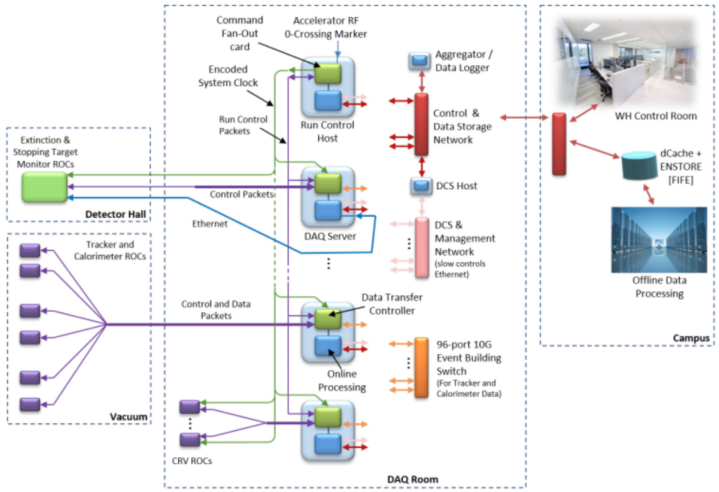

Figure 9: General Mu2e DAQ architecture

Mu2e Trigger

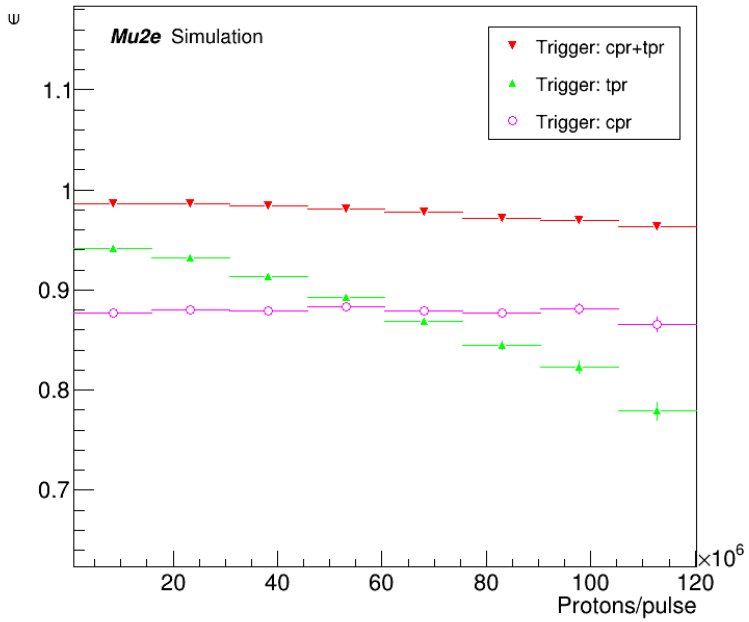

Figure 10: Trigger efficiency for $\mu^- \to e^-$ conversion on Al (red markers) relative to the offline reconstruction efficiency as a function of the proton pulse intensity. Also shown are the efficiencies of the online triggers running the individual pattern recognition algorithms: the stand-alone (*TrkPatRec*) and the calorimeter-seeded (*CalPatRec*).

The expected instantaneous trigger rate is about 60 Hz for the low beam intensity mode. The Mu2e experiment is expected to generate about 14 pB of data per year. The trigger system is optimized to keep the trigger rate below a few kHz, equivalent to $\sim$ 7 pB/year and achieve a processing time below 5 ms/event.

Status: Beamline and ST

- Delivered beam upto the diagnostic absorber in April, 2022.
- First slow extracted beam with only electrostatic septum on July 2023. Slow extraction with two septa currently in progress.
- Stopping target fully assembled. Made of 37 aluminum foils of 100 μm thickness and 75 mm radius. Supported by gold-plated tungsten wires.

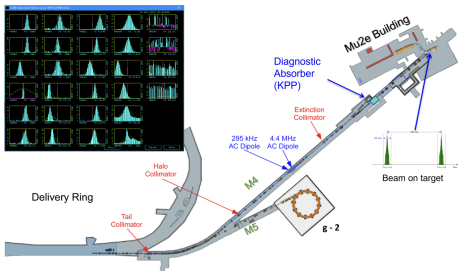

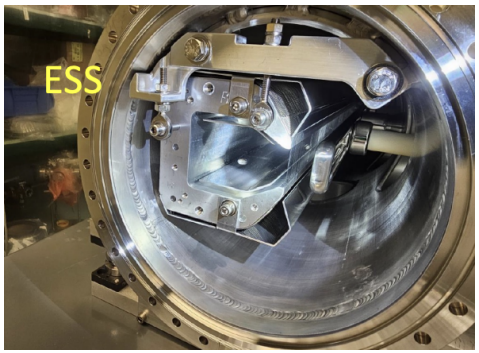

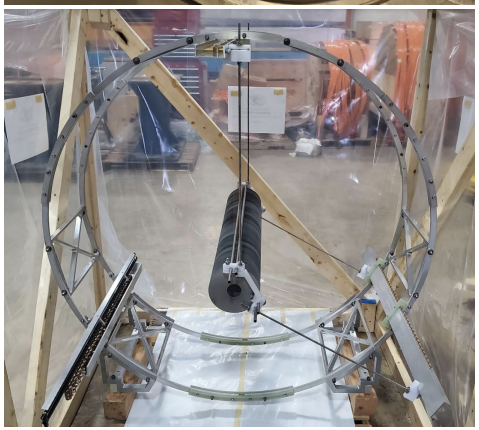

Status: Extinction Monitor

- Extinction is the suppression of protons out of the live-time detecting window.
- Mu2e physics goals requires an extinction level of 10^{-10} or better. AC dipole system upstream of the production target that deflects out-of-time protons. Fabrication of dipole magnets in progress.
- Extinction Monitor downstream the production target that measures remaining out-of-time protons. It is currently being assembled and tested in the Mu2e hall.

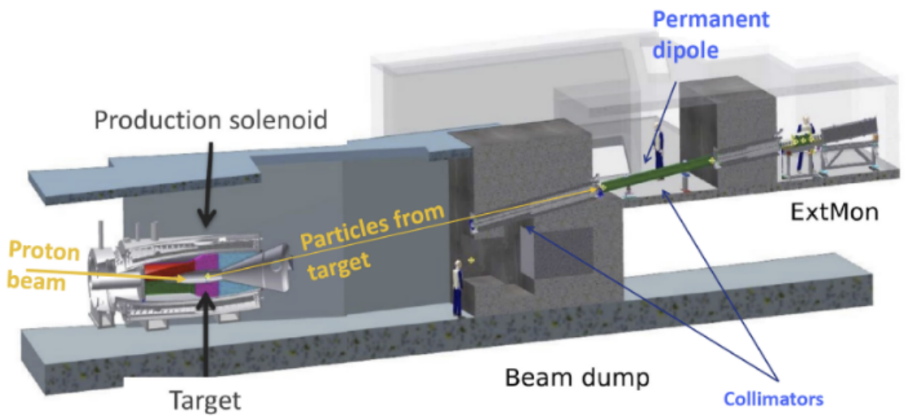

Future plans

- Mu2e II [8]: Will Utilize the PIP-II linac at Fermilab, 800 MeV proton beam (100kW on target).
- Improve sensitivity by another two orders of magnitude beyond the level Mu2e will achieve.
- Significant changes to PS and the shielding to handle higher rates as well as detector upgrades.
- Advance Muon Facility (AMF) [9]: Will also Utilize the PIP-II accelerator.
- PRISM (Phase Rotated Intense Source of Muons) system to produce muon beam with well defined momentum.

References

[1] Andre de Gouvea and Petr Vogel. Lepton Flavor and Number Conservation, and Physics Beyond the Standard Model. *Prog. Part. Nucl. Phys.*, 71:75–92, 2013.

[2] Ryuichiro Kitano, Masafumi Koike, and Yasuhiro Okada. Detailed calculation of lepton flavor violating muon-electron conversion rate for various nuclei. *Phys. Rev. D*, 66:096002, Nov 2002.

[3] Andrzej Czarnecki, Xavier Garcia i Tormo, and William J Marciano. Muon decay in orbit: spectrum of high-energy electrons. *Physical Review D—Particles, Fields, Gravitation, and Cosmology*, 84(1):013006, 2011.

[4] Collaboration Mu2e. Mu2e run i sensitivity projections for the neutrinoless muon to electron conversion search in aluminum. *Universe*, 9(1), 2023.

[5] Nikolay Atanov, Vladimir Baranov, Leo Borrel, Caterina Bloise, Julian Budagov, Sergio Ceravolo, Franco Cervelli, Francesco Colao, Marco Cordelli, Giovanni Corradi, Yuri Davydov, Stefano Di Falco, Eleonora Diociaiuti, Simone Donati, Bertrand Echenard, Carlo